RESEARCH MEMORANDUM

PRESSURE AND FORCE CHARACTERISTICS AT TRANSONIC SPEEDS

OF A SUBMERGED DIVERGENT-WALLED AIR INLET

ON A BODY OF REVOLUTION

By John A. Braden and P. Kenneth Pierpont

Langley Aeronautical Laboratory
Langley Field, Va.

CLASSIFICATION CANCELLED

Naca Res. Abs. 3/16/56
RN 98
4/23/56

NATIONAL ADVISORY COMMITTEE
FOR AERONAUTICS
WASHINGTON
May 6, 1953

NATIONAL ADVISORY COMMITTEE FOR AERONAUTICS

RESEARCH MEMORANDUM

PRESSURE AND FORCE CHARACTERISTICS AT TRANSONIC SPEEDS

OF A SUBMERGED DIVERGENT-WALLED AIR INLET

ON A BODY OF REVOLUTION

By John A. Braden and P. Kenneth Pierpont

SUMMARY

An investigation was conducted in the Langley 8-foot transonic tun-
nel on a submerged inlet with a divergent-walled approach ramp to deter-
mine flow phenomena, pressure recovery, and external forces, and to
provide correlation with available data obtained from inlets of similar
design. The two side-mounted inlets were positioned at the 25-percent-
body station of a basic body 8 inches in diameter and of fineness ratio 8.
The minimum inlet area was 16 percent of the frontal area of the model.
Data were obtained over a Mach number range from 0.60 to 1.09 for angles
of attack from $0°$ to $10.6°$, and the mass-flow ratio was varied from the
maximum that would enter the inlet down to about 0.20.

Results of the tests showed that, for mass-flow ratios between 0.40
and 0.80 at an angle of attack of $0°$ the maximum total-pressure ratio
after 2.4/1 diffusion varied from about 98 percent at a free-stream Mach
number M_O of 0.60 to about 93 percent at $M_O \approx 1.09$. At an angle of
attack of $10.6°$, the total-pressure ratio was markedly reduced, about
14 percent below the free-stream value at $M_O = 0.95$; severe flow oscil-
lations accompanied the decrease. Lift and pitching moments of the
basic body were altered very little by the addition of the submerged
inlet and changes in lift and pitching moment with mass-flow ratio were
small. The external drag at maximum mass-flow ratios was approximately
equal to that of the basic body. Variation of external drag with mass-
flow ratio was not substantially different from that of a forward-located
underslung scoop at similar test conditions.

INTRODUCTION

The use of side air inlets for fuselage-mounted engine installations generally permits a short internal ducting system to the engine and allows a maximum of internal volume for equipment. An investigation program to evaluate the pressure-recovery and force characteristics of various types of fuselage air inlets and to establish the effects of several geometric variables has been undertaken in the Langley 8-foot transonic tunnel. The first configuration tested, a forward-located underslung scoop, was reported and compared to a basic body of revolution in reference 1.

The present study was made to determine the performance at transonic speeds and angles of attack of a submerged inlet configuration similar to those reported in references 2 and 3. The inlets were installed on a fineness-ratio-8 body of revolution at the 25-percent station or midway between the nose and the maximum body diameter. This location was selected to minimize the boundary-layer and Mach number effects on the approach ramp and also from considerations of the probable wing and engine locations.

The sum of the areas for the two inlets, defined by the minimum duct area just inside the inlet, was about 16 percent of the body frontal area. Design details followed closely the recommendations for submerged inlets outlined in reference 3. Measurements included normal force, axial force, pitching moment, pressure recovery, mass flow, internal drag, and surface pressures on the several inlet components. Data were obtained for Mach numbers from 0.60 to 1.09, for angles of attack up to 10.6°, and for mass-flow ratios from the maximum that would pass the inlet to about 0.20 (throttle closed).

SYMBOLS

C_{D_e} external-drag coefficient,

$$\left(\frac{G_a}{q_0 F} + P_B \frac{B}{F} + C_{F_n}\right)\cos \alpha + \frac{G_n}{q_0 F} \sin \alpha$$

C_{F_n} internal-force coefficient, $\int c_{F_n}{}' \, d\left(\frac{A_3}{F}\right)$

C_L external-lift coefficient,

$$\frac{G_n}{q_oF} \cos \alpha - \left(\frac{G_a}{q_oF} + P_B \frac{B}{F} + C_{F_n}\right)\sin \alpha$$

C_m external-pitching-moment coefficient taken about maximum-diameter station, G_m/q_oFD

c' point mass-flow coefficient, $\rho V/\rho_oV_o$

$c_{F_n}{}'$ point internal-force coefficient, $2c'\left(\dfrac{V_3}{V_o} - \dfrac{1}{\cos \alpha}\right) + \dfrac{p_3 - p_o}{q_o}$

A duct area

B base area

D maximum body diameter

F fuselage maximum cross-sectional area

F_n internal force (positive when in a thrusting direction, negative when in a drag direction),

$$m\left(V_3 - \frac{V_o}{\cos \alpha}\right) + (p_3 - p_o)A_3$$

G_a, G_n, G_m strain-gage-measured axial force, normal force, and pitching moment

H total pressure

$\bar{H}$ mass-flow-weighted average total pressure

h inlet height

L model length

M Mach number

m mass-flow rate, ρAV

m/m_o mass-flow ratio, $m/\rho_oV_oA_1$

p static pressure

P static-pressure coefficient, $\dfrac{p - p_0}{q_0}$

q dynamic pressure, $\dfrac{1}{2}\rho V^2$

R body maximum radius

r radius

V velocity

x longitudinal distance from model nose

α angle of attack

γ ratio of specific heats, 1.4 for air

ρ mass air density

Subscripts:

o free stream

1 minimum duct area, 2.10 inches from plane of inlet

2 diffuser measurement station

3 model exit

B model base

L lip

l local

APPARATUS AND MODELS

Wind tunnel.- The Langley 8-foot transonic tunnel has a dodecagonal slotted test section and permitted continuous testing up to a Mach number of 1.09 with the present model. Details of the test section are given in reference 4, and the aerodynamic properties of the air stream are reported in reference 5.

A sketch of the model with the submerged inlet is shown mounted in the tunnel in figure 1(a) and photographic views of the model are given in figure 1(b).

Submerged-inlet model.- The submerged inlets were adapted to a modified transonic body of revolution of fineness ratio 11, which when cut off to provide an exit for internal flow had a fineness ratio of 8 (ref. 1). In order to facilitate testing and to insure that force data would be free from mechanical interference, separate similar afterbodies were used to obtain force and pressure data. Figure 2 shows the general arrangement of the inlet forebody mounted on the force and pressure afterbodies which were described in reference 1.

The combined inlet area, defined by the plane of the lip leading edge, was about 19 percent of the frontal area; whereas, the minimum inlet area totaled 0.163F. The minimum inlet areas for the right- and left-hand ducts (looking forward) as measured from templates were found to be 4.20 square inches and 4.00 square inches, respectively. The ramp center line was obtained by laying out from the basic body surface the longitudinal coordinates which had been measured from a flat surface in reference 3. The transverse ramp dimensions were laid out along circular arcs concentric with the model center line, and the side walls were formed as radial lines through the body center and the extremities of the circular arcs. The aspect ratio of the inlet at the plane of the lip leading edge was about 3.5. Details of the inlet-lip shape and approach ramp are shown in figure 3 and body and ramp coordinates are given in table I. The minimum duct area which occurred 0.72 inch downstream of the inlet plane was held constant for a distance of about 1.4 inches (1.2h) and then increased as shown in figure 3(a) to about 2.4 times the minimum duct area at the diffuser measurement station.

Instrumentation.- Instrumentation of the force and pressure after-bodies was described in reference 1. Surface pressure measurements on the forebody were made on the top, both right- and left-hand ramps, and on the outside and inside of the right-hand inlet lip (table II). Static pressure measurements on the tunnel-wall panel were made on a line 30^0 from the top center line (panel 11, ref. 5) to determine the position and strength of model-induced disturbances.

All pressure data were recorded photographically from multiple-tube manometers filled with tetrabromoethane. Force data were manually recorded from sensitive dial potentiometers and tunnel total temperatures were obtained from recording millavoltmeters. Flow visualization in the vicinity of the inlet was obtained in the form of schlieren photographs.

TESTS AND METHODS

In order to obtain schlieren photographs of the shock patterns on the ramp surfaces, the model was rotated for all the tests from its normal attitude by turning the sting-support system 90° counterclockwise (facing upstream) (see fig. 1); angle-of-attack changes were consequently made in a horizontal plane. For all the tests, the model nose was located 42 inches downstream of the slot origin to minimize the effects on the flow into the inlet of a small gradient in stream Mach number above $M_O \approx 1.02$ forward of the 50-inch station (see ref. 5).

Force and pressure data were obtained for Mach numbers from about 0.60 to 1.09, the maximum obtainable with this model, and for angles of attack of 0°, 4.3°, 7.3°, and 10.6°. In order to avoid possible boundary-layer hysteresis effects, the mass-flow ratio was varied from the maximum which would pass the inlet to the minimum of about 0.20 (throttle closed). Figure 4 shows a comparison of the maximum obtainable mass-flow ratio at 0° and 10.6° angle of attack.

Point values of the mass-flow and internal-force coefficients were calculated as described in reference 1 and average values of total-pressure ratios presented herein were weighted according to the local mass flow. The system mass-flow ratio determined from measurements at the exit is believed to be accurate to within ±0.01; whereas the individual duct mass-flow ratios at the end of the diffuser are considered to be within ±0.02. Estimated accuracy of other measurements is as follows:

p/H_O and H/H_O . . . . ±0.002

M_l . . . . ±0.006

M_O . . . . ±0.01

C_{D_e} . . . . ±0.01

C_L . . . . ±0.01

C_m . . . . ±0.02

α, deg . . . . ±0.1

Included in the estimated errors of point mass-flow ratio and external drag are those resulting from leakage into the sting fairing, which were evaluated from static tests. Second-order effects arising from assuming that $\cos \alpha = 1$ in the definition of F_n and in the computation of C_{F_n} are considered negligible. No corrections for wind-tunnel wall effects have been made. Model-induced wall-measured disturbances for the present model were compared to those of reference 1

for both the solid nose and scoop nose. These disturbances were found
to be in about the same location relative to the nose and to be of about
the same magnitude at corresponding angles of attack and Mach numbers.
It is believed, therefore, that comparisons of the data of the present
tests with those of reference 1 should afford a reasonably accurate indi-
cation of the drag, lift, and pitching-moment increments. The Reynolds
number range for these tests is shown in figure 5.

RESULTS AND DISCUSSION

The results of the investigation of the submerged inlet installa-
tion are divided so as to present external- and internal-flow character-
istics as indicated by surface pressures and internal-pressure-recovery
data; and force characteristics as indicated by normal-force, axial-
force, and pitching-moment data. Comparisons for both force and pressure-
recovery data are made with several types of inlet configurations.

Pressure Characteristics

Pressure distributions on the top center line.- Representative
pressure distributions along the top of the body at the lateral plane
of symmetry are shown in figure 6 for $\alpha = 0°$. Also shown are the curves
of the pressure distributions on the basic body (ref. 1). The principal
effect of installing the inlet was to increase the pressures in the
vicinity of the inlet and at the model exit. Beginning at $M_0 = 0.95$
for the high-mass-flow conditions, the high static-pressure field of the
inlet was felt as a strong recompression near the inlet station along
the top of the model. At $M_0 = 1.00$ and greater, this rapid pressure
rise apparently occurred through a normal shock which is believed to be
associated with the shock formation originating and extending outward
from the ramp surfaces. Data taken at angles of attack up to $10.6°$
showed effects of similar flow behavior. The effects of these abrupt
recompressions on external drag will be discussed in a later section.
Pressure increases caused by the exhaust flow and felt primarily over
the last 10 percent of the afterbody yielded reductions in the afterbody
pressure drag coefficient. A typical reduction in the pressure drag
coefficient associated with increases in mass-flow ratio was found to
be about 0.01 at $M_0 = 0.95$ from integrated values of surface pressures.
A similar reduction of 0.01 in the afterbody pressure drag coefficient
was shown for the underslung scoop of reference 1 for similar test
conditions.

Pressure distributions on ramps.- The variation of static-pressure
ratio on both right- and left-hand ramp surfaces at the center line as

a function of mass-flow ratio is presented in figures 7, 8, 9, and 10 for 0°, 4.3°, 7.3°, and 10.6° angle of attack, respectively. Schlieren photographs of the ramp flow are included in the figures.

Figure 7 shows that the pressure field of the inlet, $x/L = 0.25$, affected the ramp flow as far forward as $x/L \approx 0.12$ (about 7 inlet heights) at the lower Mach numbers, and even at $M_0 \approx 1.09$, where super-sonic velocities existed on the ramps, the flow began to meet inlet conditions as far forward as $x/L \approx 0.17$. Forward of $x/L \approx 0.12$, however, the static pressures were of about the same magnitude as those of the basic body, (ref. 1, fig. 26) and were essentially independent of mass-flow changes. The similarity of flow conditions into the two ducts even at the low-mass-flow conditions is shown by a comparison of the pressure distributions and the schlieren photographs; the slight dissimilarities shown are believed to be associated with differences in the individual duct mass-flow ratios.

At 0° angle of attack and for the maximum mass-flow ratios, sonic velocities were obtained ahead of the inlet at Mach numbers greater than about 0.90 and the resulting shock formation is shown in the schlieren photograph at $M_0 = 0.95$. Inasmuch as the pressure rise across these shocks well exceeded the pressure rise required for boundary-layer separation on a flat plate in reference 6, a localized region of separated flow on the ramp may have accompanied the appearance of these shocks. Reattachment of any separation could have occurred in the region of the strong favorable pressure gradient just ahead of the effective minimum area and the net effect would have been a general thickening of the boundary layer and a small reduction in the choking or maximum mass-flow ratio shown in figure 4 to have occurred at $M_0 \approx 0.95$. An attempt was made to correlate the position of the shock wave on the ramps with the bow wave of a nose inlet (NACA 1-40-400, ref. 7) where the Mach number on the ramps of the submerged inlet corresponded to the free-stream Mach number of the nose inlet; the location of the shocks agreed to within $\pm 0.008L$.

Operation at lower mass-flow ratios reduced the intensity of the ramp shock by forcing it forward into a region of lower Mach number. Figure 7(c) shows that although the peak local Mach number ahead of the inlet was greater than 1.00, the ramp shock became too weak to be photo-graphed by the schlieren system. A similar behavior of the ramp shock is shown at $M_0 = 0.975$ and $M_0 = 1.00$. At the minimum mass-flow ratios, the strong adverse pressure gradient just ahead of the inlet apparently gave rise to a large increase in boundary-layer thickness or possibly separation from the ramp surfaces; this is indicated at the low mass-flow ratios by the flattening of the curve at $x/L \approx 0.24$ and by the values of the diffuser static pressures shown to be below those found

for higher mass-flow ratios (i.e., fig. 7(b), compare $m/m_0 = 0.20$ with $m/m_0 = 0.61$). Increasing the Mach number appeared to aggravate this condition and caused it to become evident at higher mass-flow ratios (see fig. 7(e), $m/m_0 = 0.39$).

As the angle of attack was increased (see figs. 8 to 10), the ingested flow became increasingly disturbed at all mass-flow ratios by the vortices induced by spillage over the ramp side walls. Up to an angle of attack of 7.3^0, the increased intensity of the vortex and possible separation induced at the lower side walls caused gradual reductions in the static-pressure ratios just forward and downstream of the inlet. Operation at 10.6^0, however, caused abrupt decreases in the static pressures throughout the ducts indicating extensive regions of nonuniform flow. Furthermore, unsymmetrical flow conditions between the two inlets are evidenced by the larger variations in the duct static-pressure ratios (see fig. 10(b)).

Static-pressure distributions on inlet lip.- Static-pressure distributions on the inside of the right-hand inlet lip (fig. 11(a)) at $\alpha = 0^0$ show that for all Mach numbers a small supersonic region existed near the lip leading edge for the high mass-flow ratios. The maximum local indicated Mach number decreased from about 1.2 at $M_0 = 0.95$ to about 0.6 as the mass-flow ratio was reduced from choke to about 0.70. Below $m/m_0 = 0.70$, however, the maximum local Mach number first decreased by about 0.10 and then increased by about the same amount as the minimum mass flow was approached. This effect is an indication of the flow asymmetry of the ingested air at the low mass-flow ratios.

A study of figure 11(b) for $\alpha = 10.6^0$ and additional data at 4.3^0 and 7.3^0 showed that the effect of angle of attack was to increase the local Mach number around the inside of the lip at the center line for all test conditions; a further indication of this is given in a later figure of point-mass-flow-ratio and impact-ratio contours in the diffuser.

Pressure distributions along the outside of the lip at the center line (see fig. 12) show that at the low mass-flow ratios a narrow region of high superstream velocities occurred around the leading edge for Mach numbers of 0.60 and 0.80; these velocities became supersonic at $M_0 = 0.80$. At all higher Mach numbers, important increases in the length of this region occurred. At $M_0 = 0.95$ and greater, a weak compression followed by a region of increasing velocities is shown to have occurred just back of the lip leading edge. It is believed that this disturbance is similar to the weak shock formations found on the leading edges of supersonic airfoils operating under lifting conditions. Reference 8 states that the conditions under which the weak shocks formed on the supersonic airfoils

tested appeared to be the existence of supersonic velocities in the
vicinity of the leading edge and a highly localized separated region
originating at the leading edge and extending only a short distance
rearward. Operation at the high mass-flow ratios reduced the effective
angle of attack of the lip and thereby prevented the formation of this
disturbance. At $M_O = 0.95$ and 1.00, and for mass-flow ratios from
about 0.20 to 0.60, recompression to the body static pressures rearward
of the lip apparently occurred through a system of small shocks. At
higher mass-flow ratios, the figure indicates that normal shocks may
have been present. At an angle of attack of 10.6^O (fig. 13), the maxi-
mum local Mach number at the lip center line was reduced by the effec-
tive sweep of the lip leading edge and resulted in a much more uniform
pressure distribution. However, it may be noted that at angles of
attack, minimum pressures were not necessarily measured at the center
line but may have occurred elsewhere along the lip span. Large cross
flows around the body surface substantially reduced the static pressure
levels rearward of the lip $(x/L > 0.30)$ and a rapid rise from the lip to
the body surface pressures such as found at 0° was not required.

Internal-pressure recovery.- The variation of the mass-flow-weighted
total-pressure recovery at the diffuser measurement station for each duct
as a function of the system mass-flow ratio at the test angles of attack
are presented in figure 14; corresponding diffuser static-pressure ratios
are given in figure 15. The curves have been faired through the system
mass-flow-weighted total-pressure recovery instead of the individual duct
values. Large deviations from the mean curve at low mass-flow ratios
resulted primarily from unstable flow conditions discussed later. Point-
mass-flow-ratio and impact-pressure-ratio contours at the diffuser meas-
urement station are shown in figure 16.

At 0° angle of attack, the maximum average total-pressure recovery
occurred at a mass-flow ratio of from 0.60 to 0.70 and was approximately
$0.98H_O$ at a Mach number of 0.60; a gradual decrease occurred with
increasing Mach number to about $0.96H_O$ at $M_O = 1.00$. At the highest
test Mach numbers the maximum pressure recovery decreased to $0.93H_O$.
These additional losses at supersonic speeds are understandable and arise
from several primary sources: the loss through the bow shock ahead of
the model nose, the loss through the shock on the ramp surface, boundary-
layer growth, and the generally increased level of viscous losses due to
the higher local velocities throughout the system as the stream Mach
number increased. The 2- to 3-percent decrease in recovery below the
maximum at low mass-flow ratios was accompanied by some flow dissymmetry
between the two ducts. A general thickening of the boundary layer or
possible separation from the ramp surface together with the change from
translational to rotational energy which resulted from the generation of
vortices from the ramp side walls would readily account for these
decreases.

At high mass-flow ratios, the total-pressure recovery decreased about 3 percent below the maximum value as the choking mass-flow ratio was approached. The abrupt decrease in recovery at the maximum mass-flow ratio is characteristic of an inlet without extensive separation ahead of the minimum area station.

At Mach numbers below 0.90, operation at angles of attack up to 7.3° showed gradually increasing losses associated with either boundary-layer separation from the lower ramp wall or energy losses from the strong ramp vortices. Higher Mach numbers, however, magnified the effects of angle-of-attack change and the total-pressure recovery decreased rapidly. At 10.6° angle of attack, extensive losses associated with the flow over the lower ramp side wall caused large reductions in recovery at all Mach numbers and mass-flow ratios. For example, at $M_O = 0.95$ and $m/m_O = 0.80$, increasing the angle of attack from 0° to 7.3° caused a 5.5-percent reduction in total-pressure ratio, whereas an additional 3.3° ($\alpha = 10.6^\circ$) caused a 4.5 percent greater loss over that at 7.3°. In addition to these large losses in total-pressure ratio at 10.6°, flow oscillations in the two ducts were present at all but the highest mass-flow ratios.

Figure 15 shows that, for $\alpha = 0^\circ$ and in the high-mass-flow range, the static-pressure recovery decreased with increasing mass-flow ratio; whereas, at 10.6°, the high Mach number conditions indicate a tendency toward a reversal in the slope of the curve. According to reference 9, this behavior of the static-pressure-recovery curves is an indication of internal-flow instability in a twin-duct system which is primarily a function of the static-pressure-recovery characteristics at the juncture of the two ducts. Flow oscillations could occur when the model is operating through a range of mass-flow ratios for which the static-pressure recovery increases with increasing mass-flow ratio. At $\alpha = 0^\circ$, figure 15 indicates that conditions for instability existed at mass-flow ratios below 0.50 at all Mach numbers. From the static-pressure recoveries, operation at angles of attack up to 7.3° apparently improved the range of flow stability, but as the angle of attack was increased from 7.3° to 10.6° unstable conditions were possible over a wide range of mass-flow ratios at Mach numbers greater than 0.95. At $M_O \approx 1.09$, visual observations made during the tests verified the unstable conditions indicated by figure 15 at mass-flow ratios as high as 0.70, and it was estimated that the frequency of the oscillation was about 4 cycles per minute. The presence of high-frequency oscillations could not be observed because of the relatively slow response of the system.

Internal performance and pressure-recovery characteristics at $M_O \approx 1.09$ are also indicated by the point-mass-flow-ratio and impact-pressure-ratio contours in figure 16. At 0° angle of attack and low mass-flow ratios, the figure shows that in this unstable flow range

most of the air was carried by the left-hand inlet. At a mass-flow
ratio of 0.95 most of the air flow passed the diffuser measurement sta-
tion close to the top and bottom surfaces of the lateral-support strut
fairing. Separation from the lower ramp side wall at $\alpha = 10.6^{\circ}$ caused
most of the flow to be always carried by the upper halves of the ducts;
increasing the mass-flow ratio improved the symmetry of the flow. The
impact-pressure-ratio contours for 0° show about the same characteristics
of flow behavior as shown by the point-mass-flow-ratio contours. At
10.6°, separation on the ramp is reflected by the 5 to 10 percent lower
impact-pressure ratios shown for the bottom halves of the ducts.

Aerodynamic Forces

Lift and pitching moment.- External lift and external pitching
moment as used herein consist of all of the effects of pressure and vis-
cous forces on the external body surface and the entering stream tube
surface except those forces which are common to both surfaces. External
lift was calculated by the addition of the vertical components of the
thrust forces and base pressures to the strain-gage data. The external
pitching moment, taken about the maximum-body-diameter station, was com-
puted from the measured value on the assumption that the exhaust flow
acted in an axial direction through the pitching-moment center. It may
be noted that the numerical values obtained from the foregoing defini-
tion of external pitching moment do not directly reflect the pressure
changes on the washed surface ahead of the inlet. Included in figures 17
and 18 of lift and pitching moment are the values obtained for the basic
body with tail cone at corresponding Mach numbers (ref. 1). Figure 17
shows that the addition of the inlet to the basic body increased the
lift coefficient throughout the Mach number and angle-of-attack range
and that the ingestion of air yielded still further increases in lift.
The pitching-moment characteristics (fig. 18) are seen to have been
about the same as those found for the basic body through both the Mach
number and angle-of-attack range. No important changes in pitching
moment occurred with changes in mass flow and calculations indicated a
rearward shift in the pitching-moment center with increases in mass-flow
ratio.

External drag.- The definition of external drag as applied to the
submerged inlet is analagous to that of the lift and pitching moment in
that it consists of the sum of all the pressure and viscous forces on
the external body surface and the entering stream-tube surface, except
those forces which are common to both surfaces. External-drag coeffi-
cients along with the internal- and base-force coefficients have been
plotted in figure 19 as a function of mass-flow ratio through the test
Mach number and angle-of-attack range. It is shown in the figure that
the minimum drag occurred at the maximum mass-flow ratio; the magnitude
of the minimum drag value is approximately equal to that of the basic

body of reference 1. Therefore, shocks on the ramps, the top and the sides of the body, and on the lip outside occurring at these high mass-flow ratios are believed to have caused no important changes in the external drag. Reductions in mass-flow ratio, however, resulted in substantial increases in the value of the external drag. These increases are associated with steeper adverse pressure gradients on the lips and the larger viscous effects at the reduced mass-flow ratios. A more detailed discussion of the source of this adverse characteristic is given in reference 1. The measured drag for similar test conditions corresponded closely to the values obtained for the underslung scoop of reference 1 and are substantially greater at reduced mass-flow ratios than those reported for the open-nose inlets of reference 7. It is presumed, therefore, that the pressure rise on the ramps occurring with reductions in mass-flow ratio yielded increases in the thrust forces on the ramp side walls. These thrust forces thus acted to oppose the drag forces associated with decelerating the ingested air and reduced the lip suction forces required for a momentum balance.

The variation of external drag is shown in figure 19 to be small up to 7.3° angle of attack. The large increase occurring between 7.3° and 10.6°, 50-percent increase over C_{D_e} for 0° at $M_0 = 0.95$ and $m/m_0 = 0.80$, is indicative of the large cross-flow-separation effects on the afterbody. However, at 10.6° the external-drag values at moderate mass-flow ratios showed no large increases above those found for the basic body under similar test conditions.

Performance Comparisons

Total-pressure recovery.- The internal-total-pressure recovery as a function of the mass-flow ratio for the submerged inlet is compared in figure 20 with the total-pressure recovery of the underslung scoop of reference 1, a submerged scoop of reference 10 which was similar to the present model, and the NACA 1-40-200 nose inlet of reference 7 for 0° and 10.6° angle of attack.

It is shown in figure 20 that for 0° angle of attack and for a Mach number of 0.80, the maximum total-pressure recovery of the submerged inlet was about 2 percent below that of the underslung scoop, which had a recovery above $0.97H_0$ throughout a mass-flow range from $m/m_0 = 0.20$ to 1.00. At high Mach numbers, however, the submerged-inlet installation caused reductions in recovery of about 4 percent below those for the underslung scoop, and furthermore, resulted in lower choking values of mass-flow ratio than for the other two types of inlets shown. At an angle of attack of 10.6°, the underslung scoop sustained no adverse effects and the nose inlet incurred only small total-pressure losses

from separation at the lower inner-lip fairing. The submerged-inlet
installation, however, in addition to showing reductions in total-
pressure recovery of about 20 percent below that achieved by the under-
slung scoop and lower choking mass-flow ratios, was subject at the high
Mach numbers to serious flow oscillations at mass-flow ratios as high
as 0.70. The improved recovery at the low mass-flow ratios of the pres-
ent model compared to that of the submerged inlet of reference 10 may
have resulted from the difference in the inclination of the ramp walls
and the relative location of the inlets. Similar improvements in total-
pressure recovery at $m/m_o \approx 0.80$ were shown in reference 11 wherein
the ramp side walls were inclined outward relative to the ramp surface.
Canting the inlets downward several degrees may yield increases in pres-
sure recovery for high angles of attack at the cost of reductions at the
high-speed condition. If these reductions could be tolerated, a range
of moderate pressure recoveries could be extended to high angles of
attack. It may be concluded, however, that the pressure-recovery per-
formance of this adaptation of the submerged inlet at 10.6^o angle of
attack is greatly inferior to that of the underslung scoop, and even at
0° angle of attack, it cannot achieve the performance realized by the
other two types of inlet configurations without additional flow controls.

Lift and pitching moments.- The effect of installing the submerged
inlet on a body of revolution is compared in figure 21 to the underslung
scoop (ref. 1) in terms of lift and pitching-moment coefficients at
$M_o = 0.95$ and $m/m_o = 0.80$. It is seen in the figure that the addition
of the submerged inlet to the basic body resulted in an increase in lift
coefficient of about 0.05 throughout the angle-of-attack range whereas
the lift coefficient of the underslung scoop is seen to be about the
same as that of the basic body at the lower angles of attack and approxi-
mately equal to that of the submerged inlet at 10°. This 0.05 increment
in lift coefficient based on frontal area would be regarded as insignif-
icant when applied to a real airplane; for instance, it would amount to
about 0.003 when based on the area of a typical wing adapted to this
body. The symmetrically located submerged inlets show practically the
same value of pitching-moment coefficient as found for the basic body at
all angles of attack. As would be expected, the underslung scoop,
located below the body center line, shows a nose-down decrement in
pitching moment of about 0.2 when compared to the basic body through the
angle-of-attack range. This decrement in pitching-moment coefficient
would be about only 0.01 when referred to the aforementioned wing-body
combination.

External drag.- A comparison has been made (fig. 22) of the varia-
tion of external drag as a function of mass-flow ratio at $M_o = 0.80$
of all the available external drag data of similar submerged inlets
obtained in wind tunnels (see refs. 3 and 12 to 14). Widely diverse
test techniques and model configurations were used for these tests.

Because such differences existed, the external-drag values of all the models were adjusted to correspond to the same values at a mass-flow ratio of about 1.00 and the data are therefore shown as an increment of external drag due to a reduction in mass-flow ratio. The agreement is generally good and the trend shown agrees with that obtained from momentum considerations of the flow as discussed in reference 1.

The effect on external drag of the addition of the submerged inlet to the basic body with tail cone is shown in figure 23 at 0° and 10.6^O angle of attack for $m/m_O = 0.80$. Also included in the figure is the external drag data for the underslung scoop. It is seen that the external drag of the submerged scoop as well as that of the underslung scoop at both 0° and 10.6^O angle of attack is approximately equal to that of the basic body throughout the Mach number range. Also, no important changes in the drag-rise Mach number are shown to have resulted from the installation of either inlet. It was shown in reference 1 that up to $M_O = 1.1$ the underslung scoop was at least as good dragwise at high mass-flow ratios as the NACA 1-series nose inlets of comparable inlet area. Furthermore, it appears that for these test conditions, at least, large geometric differences (i.e., lip shape and inlet location) have resulted in only minor changes in external drag.

CONCLUDING REMARKS

An investigation in the Langley 8-foot transonic tunnel of a divergent-walled submerged inlet tested through a Mach number range from 0.60 to 1.09 and angles of attack up to 10.6^O yielded the following results:

1. At 0° angle of attack, the maximum total-pressure recovery after 2.4/1 diffusion occurred at a mass-flow ratio m/m_O of about 0.60 and was 98 percent at a free-stream Mach number M_O of 0.60 but decreased to about 93 percent at $M_O \approx 1.09$.

2. At 10.6^O angle of attack, extensive total pressure losses associated with the flow over the lower ramp side walls occurred at all Mach numbers and were accompanied by severe flow oscillations; at $M_O = 0.95$ and $m/m_O = 0.80$ these losses were about 14 percent of the free-stream value.

3. The addition of the submerged inlet to the basic body was shown to have resulted in only minor changes in the lift and pitching-moment coefficients.

4. The external drag at high mass-flow ratios was approximately equal to that of the basic body through the Mach number and angle-of-attack range.

5. A comparison of the submerged scoop with a forward-located underslung scoop indicated that large geometric changes such as lip shape and inlet location resulted in only minor changes in external drag as a function of mass-flow ratio.

6. A comparison of the pressure-recovery characteristics of the submerged inlet with those of an underslung scoop and a nose inlet indicated that the performance of this adaptation of the divergent-walled submerged inlet was greatly inferior at high angles of attack; even at 0° this submerged inlet did not realize the pressure-recovery performance achieved by the other two types of inlet configurations.

Langley Aeronautical Laboratory,
    National Advisory Committee for Aeronautics,
        Langley Field, Va.

REFERENCES

1. Pierpont, P. Kenneth, and Braden, John A.: Investigation at Transonic Speeds of a Forward-Located Underslung Air Inlet on a Body of Revolution. NACA RM L52K17, 1953.

2. Mossman, Emmet A., and Randall, Lauros M.: An Experimental Investigation of the Design Variables for NACA Submerged Duct Entrances. NACA RM A7I30, 1948.

3. Hall, Charles F., and Barclay, F. Dorn: An Experimental Investigation of NACA Submerged Inlets at High Subsonic Speeds. I - Inlets Forward of the Wing Leading Edge. NACA RM A8B16, 1948.

4. Wright, Ray H., and Ritchie, Virgil S.: Characteristics of a Transonic Test Section With Various Slot Shapes in the Langley 8-Foot High-Speed Tunnel. NACA RM L51H10, 1951.

5. Ritchie, Virgil S., and Pearson, Albin O.: Calibration of the Slotted Test Section of the Langley 8-Foot Transonic Tunnel and Preliminary Experimental Investigation of Boundary-Reflected Disturbances. NACA RM L51K14, 1952.

6. Donaldson, Coleman duP., and Lange, Roy H.: Study of the Pressure Rise Across Shock Waves Required To Separate Laminar and Turbulent Boundary Layers. NACA TN 2770, 1952.

7. Pendley, Robert E., Milillo, Joseph R., and Fleming, Frank F.: An Investigation of Three NACA 1-Series Nose Inlets at Subsonic and Transonic Speeds. NACA RM L52J23, 1953.

8. Lindsey, W. F., Daley, Bernard N., and Humphreys, Milton D.: The Flow and Force Characteristics of Supersonic Airfoils at High Subsonic Speeds. NACA TN 1211, 1947.

9. Martin, Norman J., and Holzhauser, Curt A.: Analysis of Factors Influencing the Stability Characteristics of Symmetrical Twin-Intake Air-Induction Systems. NACA TN 2049, 1950.

10. Selna, James, and Schlaff, Bernard A.: An Investigation of the Drag and Pressure Recovery of a Submerged Inlet and a Nose Inlet in the Transonic Flight Range With Free-Fall Models. NACA RM A51H20, 1951.

11. Taylor, Robert A.: Some Effects of Side-Wall Modifications on the Drag and Pressure Recovery of an NACA Submerged Inlet at Transonic Speeds. NACA RM A51L03a, 1952.

12. Seddon, J.: Fuselage and Air Intake Drag Measurements at Low Mach
      Number on a Model of a Single-Engined Jet Aircraft With Exit at
      the Tail. TN No. Aero. 2051, British R.A.E., May 1950.

13. Holzhauser, Curt A.: An Experimental Investigation at Large Scale
      of an NACA Submerged Intake and Deflector Installation on the
      Rearward Portion of a Fuselage. NACA RM A50F13, 1950.

14. Delany, Noel K.: An Investigation of Submerged Air Inlets on a
      1/4-Scale Model of a Typical Fighter-Type Airplane. NACA RM A8A20,
      1948.

TABLE I

SUBMERGED INLET FOREBODY DESIGN COORDINATES

$\left[\text{See fig. 3(a)}\right]$

FUSELAGE COORDINATES	
x, in.	r_f, in.
0	0
.320	.222
.480	.286
.800	.411
1.600	.693
3.200	1.157
4.800	1.549
6.400	1.892
9.600	2.489
12.800	2.966
16.000	3.326
19.200	3.591
22.400	3.776
25.600	3.901
28.800	3.978
32.000	4.000
37.600	3.965
43.200	3.863
48.800	3.688
54.400	3.419
60.600	3.003
64.000	2.600
L.E. radius = 0.048	

RAMP COORDINATES		
x, in.	r_r, in.	z, in.
3.280	1.181	0.115
4.130	1.368	.182
4.540	1.444	.220
6.179	1.634	.347
7.810	1.753	.485
9.450	1.858	.640
11.087	1.927	.878
12.725	1.949	1.146
14.362	1.942	1.352
16.000	1.917	1.380

TABLE II

MEASURED LOCATIONS OF SURFACE ORIFICES

x, in.				
Top center line	Ramp center line		Lip center line	
	Right	Left	Outside	Inside
0.02	2.02	2.00	16.00	16.00
4.01	4.00	3.99	16.24	16.25
8.02	6.01	5.99	16.49	16.49
12.00	8.00	7.99	[a]16.73	16.74
16.00	9.00	9.00	16.98	16.98
19.98	9.99	10.00	17.48	
23.98	11.00	11.01	17.96	
28.00	11.99	12.01	18.95	
30.50	13.00	[a]13.00	20.42	
33.25	14.00	14.01	22.39	
34.75	15.00	15.01	24.35	
36.26	16.00	16.01	25.99	
38.01	18.00	18.00	28.00	
39.76	22.02	[a]22.00	30.00	
41.14	26.01	26.01		
44.62				
46.25				
48.14				
50.01				
52.02				
54.00				
55.90				
[a]57.77				
[a]60.01				
63.52				

[a]Defective during entire test.
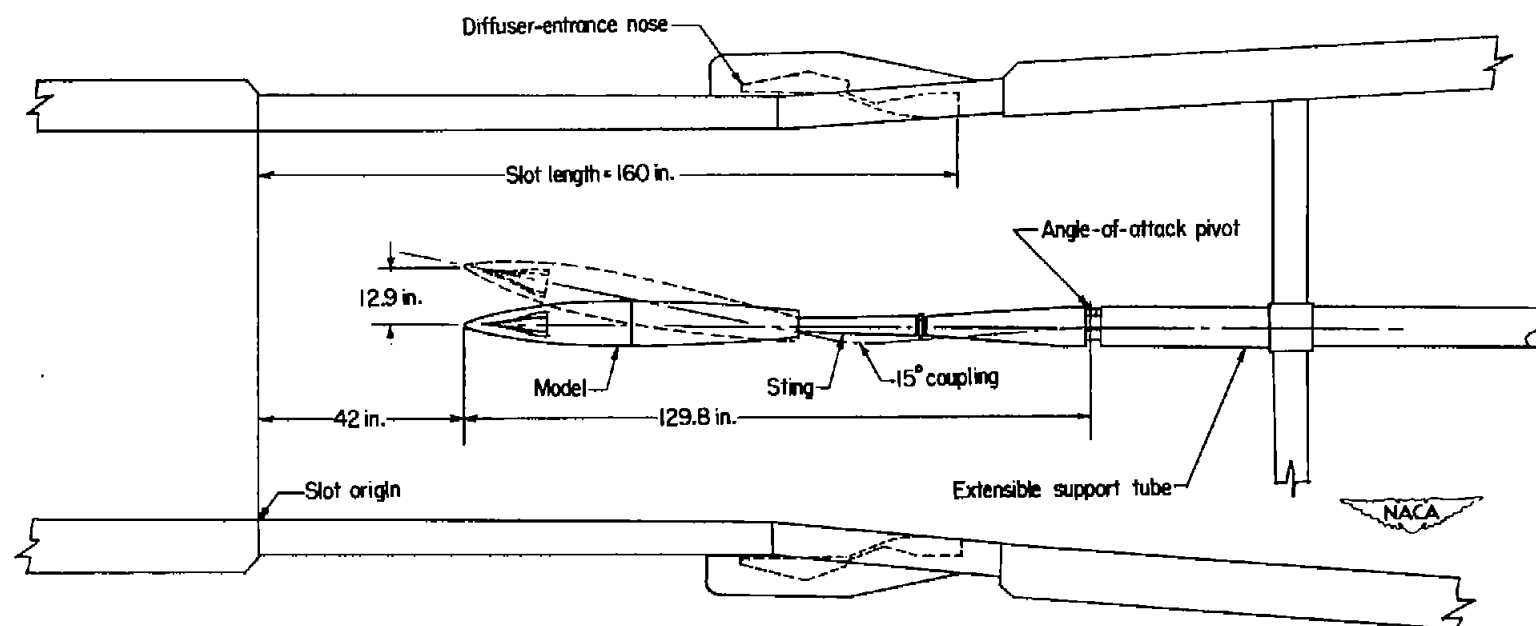
(a) Sketch showing model rotated 90° from test attitude.

Figure 1.- General arrangement of inlet model mounted in the Langley 8-foot
transonic tunnel.
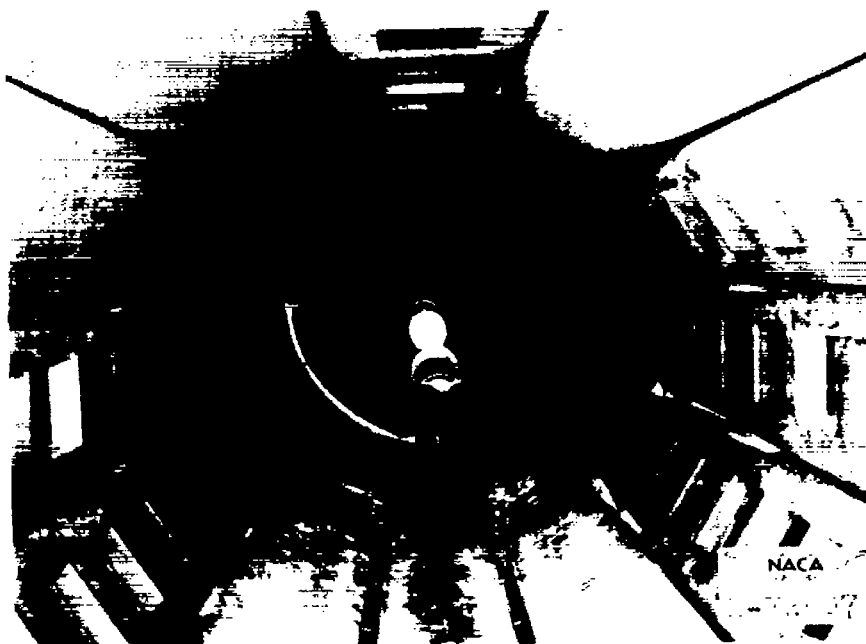
(b) Photographs of model in tunnel.

Figure 1.- Concluded.

Front view labels: ORIFICES — FRONT VIEW

Top section labels: PARTING LINE — THROTTLE — MOTOR WELL — AFTERBODY — 5.154" — EXIT RAKES — D$_{MAX}$=8.022" — STA. 43.20 — 2.500" — 5.200" — .020" — 16.00" — 32.000" — 31.994" — 63.994" — STA. 0"

X=32.00" section:
70° 50° 40° 30° 15°

X=32.00"

TUBE RADII FROM ₵ (IN)

| 2.43 |
| 2.66 |
| 2.86 |
| 3.05 |
| 3.23 |
| 3.40 |
| 3.56 |

• STATIC
○ TOTAL HEAD

X=43.20" section: THROTTLE OPEN — BOUNDARY LAYER DUCT — THROTTLE CLOSED — NACA
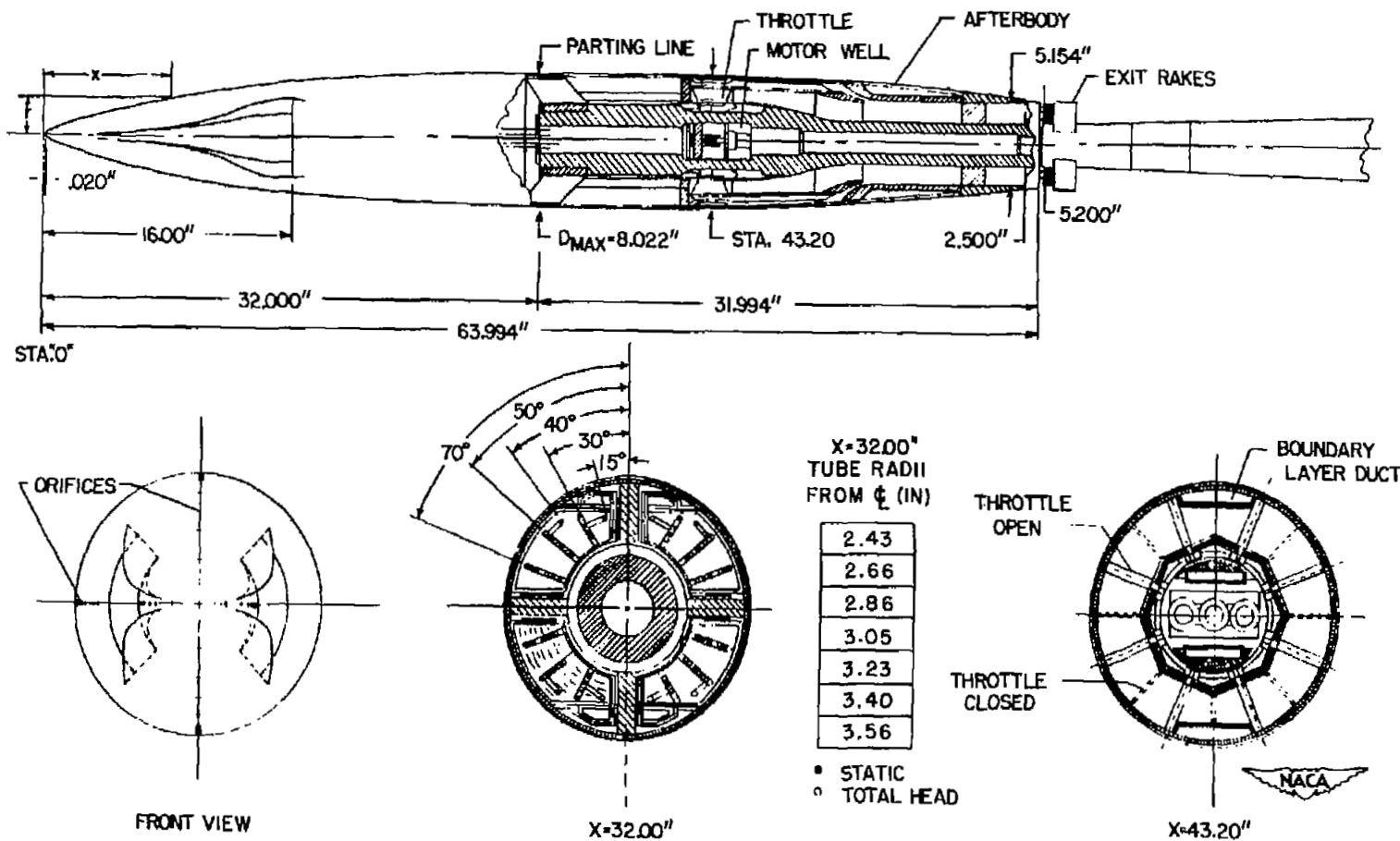
(a) Section through pressure afterbody.

Figure 2.- Model details.

X=0.02" X=17.00" X=24.00" X=32.00" X=63.50"

MAIN SUPPORT STRUT — PRESSURE RECOVERY RAKES
THROTTLE VANE
CRUCIFORM EXIT RAKE

DRAG BEAM — THROTTLE DRIVE MOTOR
STING FAIRING SUPPORT STRUT

LIFT & MOMENT BEAMS

FOREBODY ← → AFTERBODY

BOUNDARY LAYER CONTROL DUCT EXIT (PROVIDED FOR LATER TEST)

MAX. BODY DIAM.

55°
46°6'
46°6'
40°
55°
45°

TUBE RADII FROM ℄ (IN)
2.52
2.80
3.05
3.30
3.51
• STATIC
∘ TOTAL HEAD

TUBE RADII FROM ℄ (IN)
1.30
1.44
1.61
1.76
1.90
2.03
2.15
2.26
2.37
2.48
• STATIC
∘ TOTAL HEAD

X=17.00" X=24.00" X=32.00" X=63.50"

(b) Cutaway of model on force afterbody.

Figure 2.- Concluded.

L-77963

ORIFICE LOCATIONS
TABLE II

16.00"

8.00"

3.280"

31.98"

X = 16.00"

46°6'

LIP REFERENCE
LINE

3.093"

z

INTERNAL DUCTING VARIATION

$A_1 = 3.927$ sq in.

6° CONE

LIP L.E.

A/A_1

x/L

LIP REFERENCE LINE

DESIGN
LIP COORDINATES

x_1	u	l
0.000	0.000	0.000
.102	.110	.098
.205	.153	.125
.307	.185	.143
.410	.214	.155
.512	.238	.162
.614	.259	.167
.717	.276	.168
.819	.292	
.921	.308	
1.024	.318	
1.126	.329	
1.229	.340	.168

NACA

LIP DETAILS
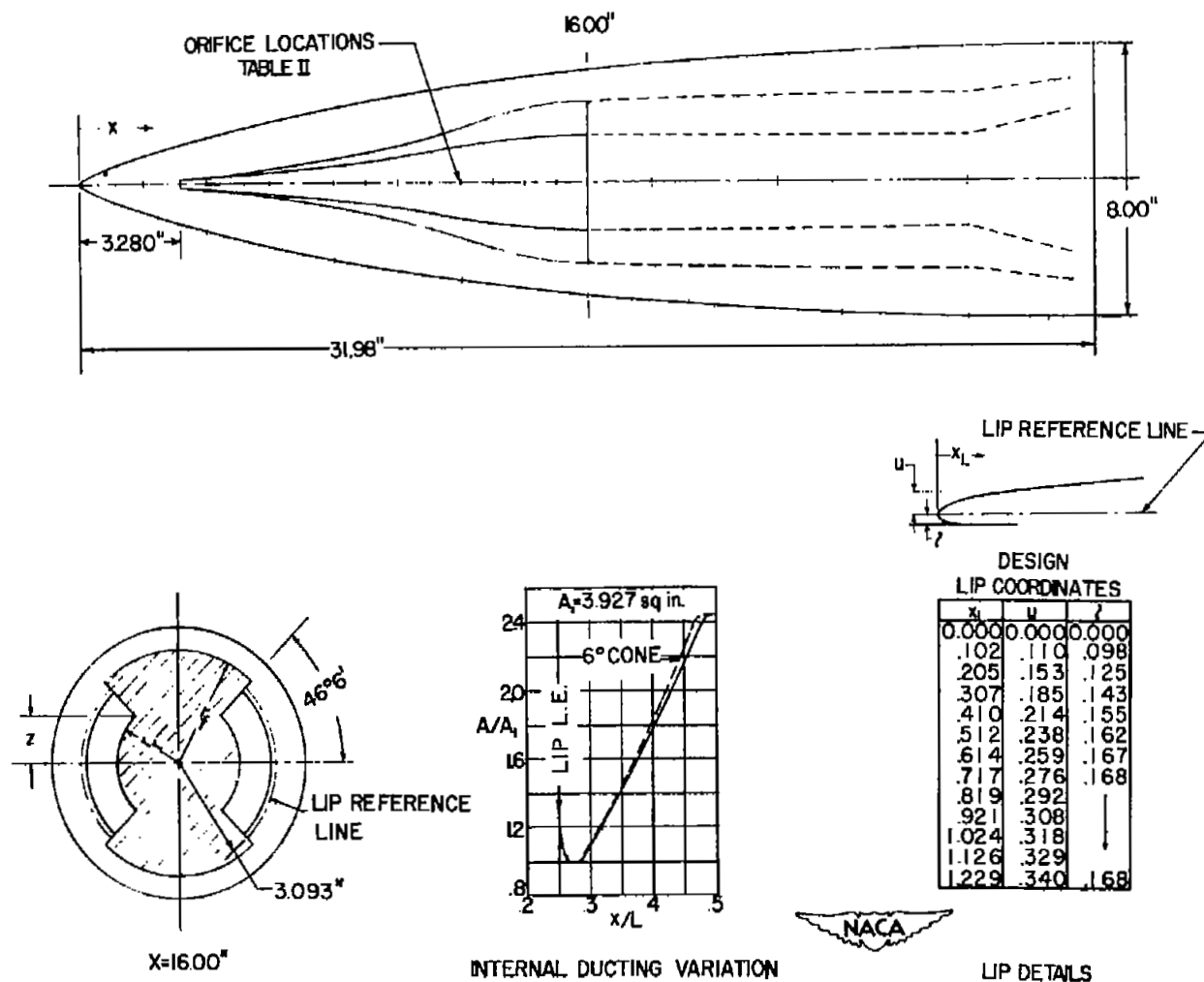
(a) Inlet and lip.

Figure 3.- Details of the submerged inlet.

(b) Photograph of the approach ramp.

Figure 3.- Concluded.
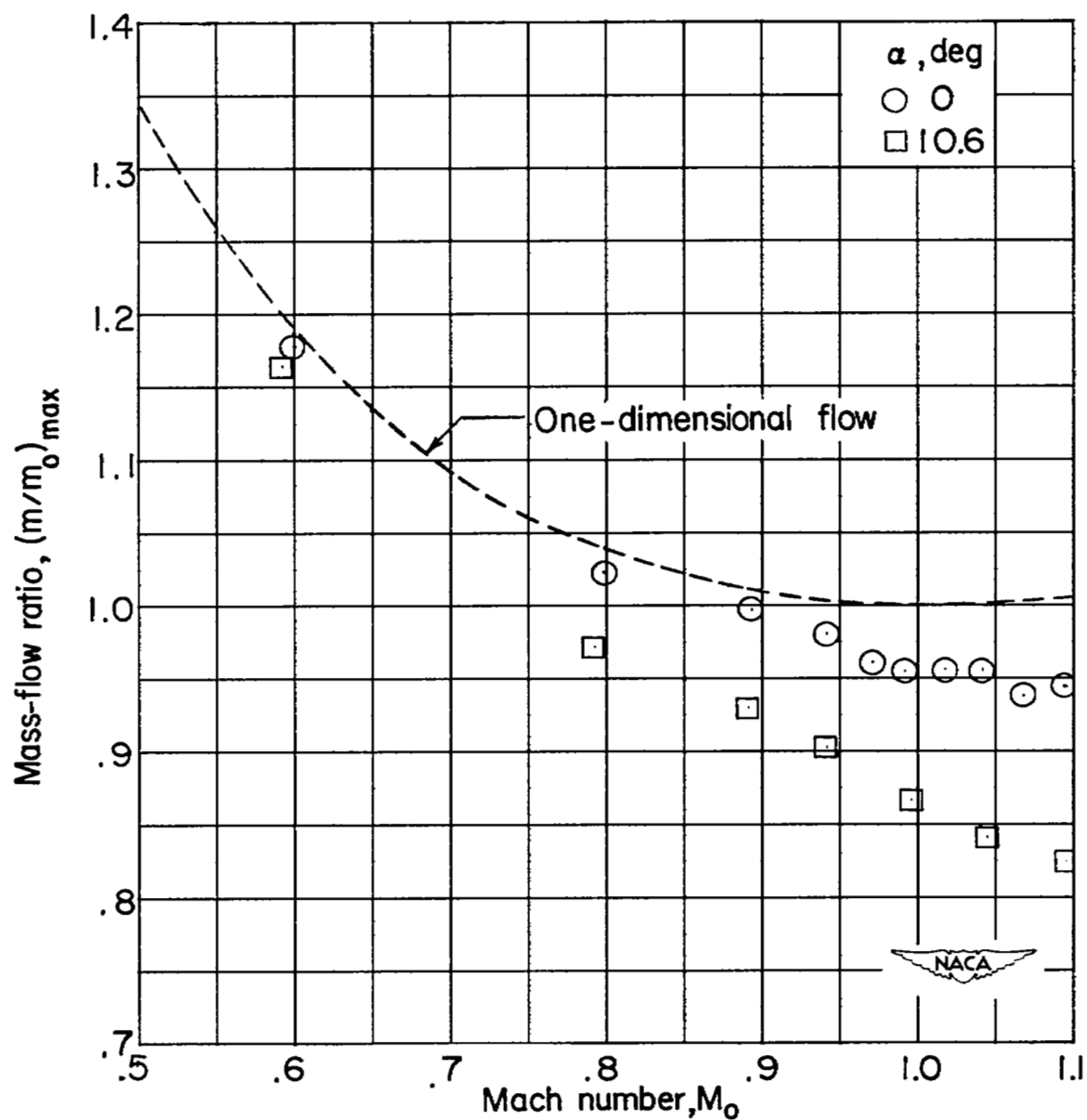
Figure 4.- Comparison of calculated and measured maximum obtainable mass-
flow ratios.
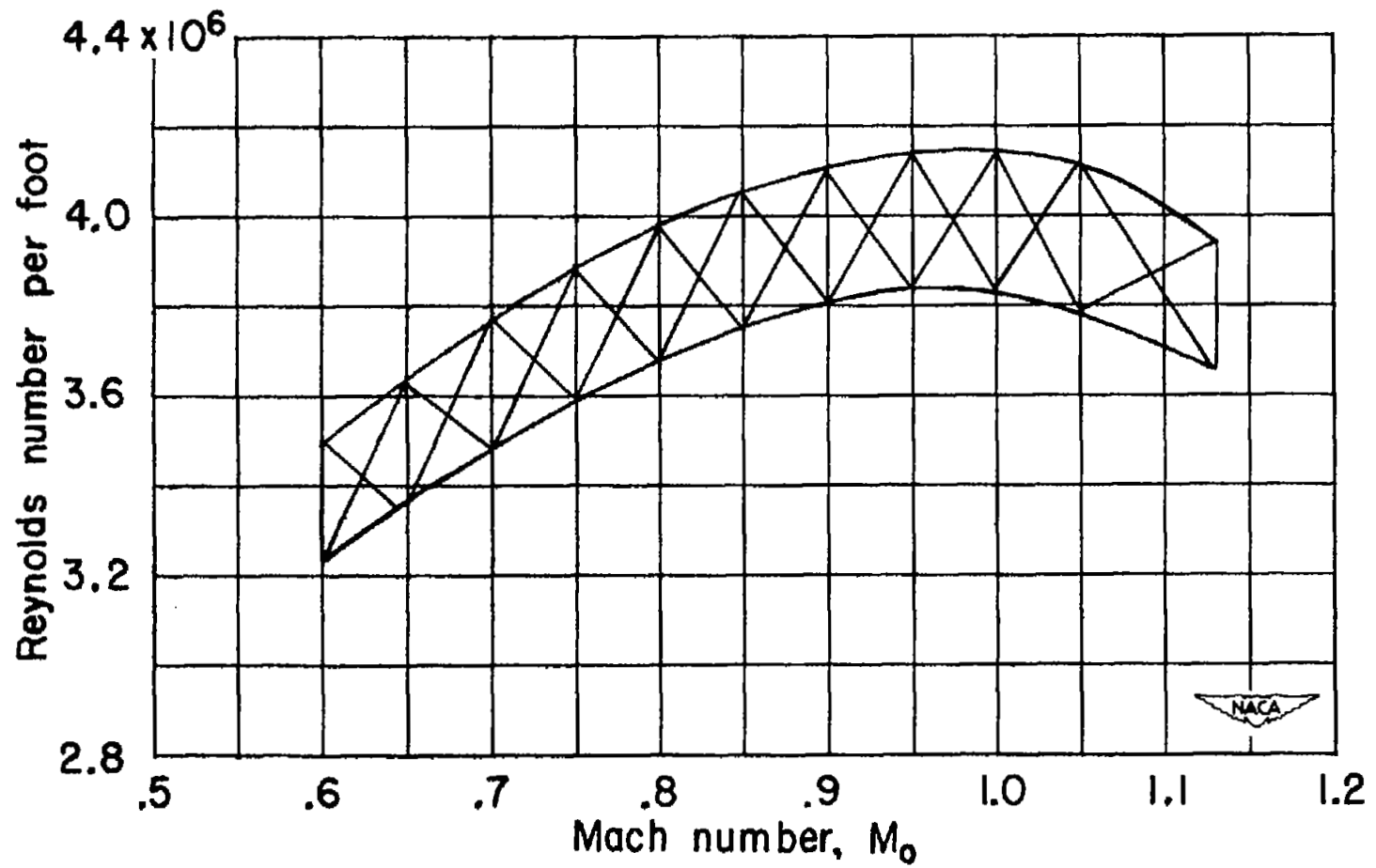
Figure 5.- Reynolds number variation per foot lineal dimension in the Langley 8-foot transonic tunnel.
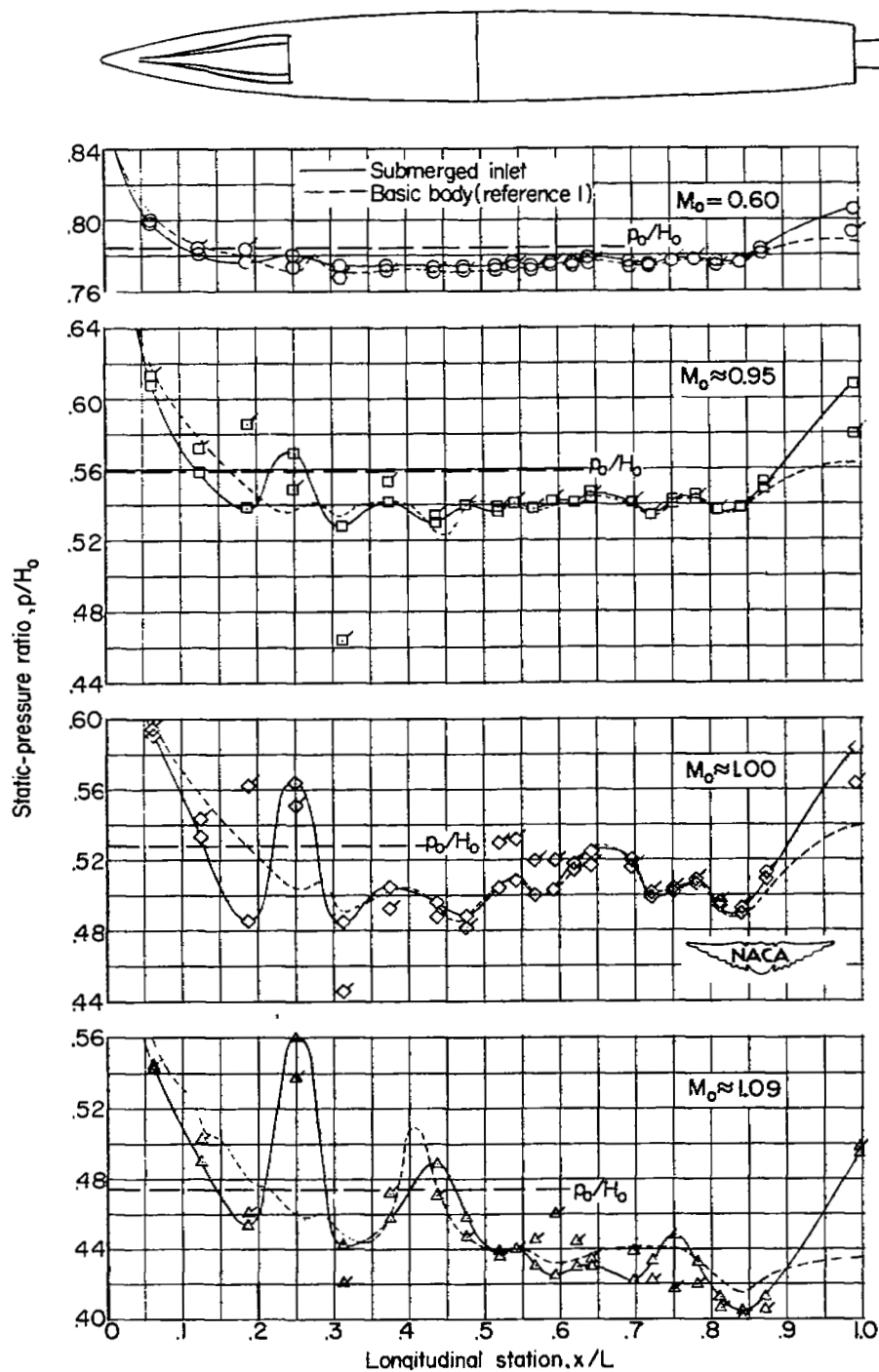
Figure 6.- Comparison of static-pressure ratios along the top center
line of the submerged inlet and basic body at the maximum mass-flow
ratios. $\alpha = 0°$. (Flagged symbols for a mass-flow ratio of about 0.3.)
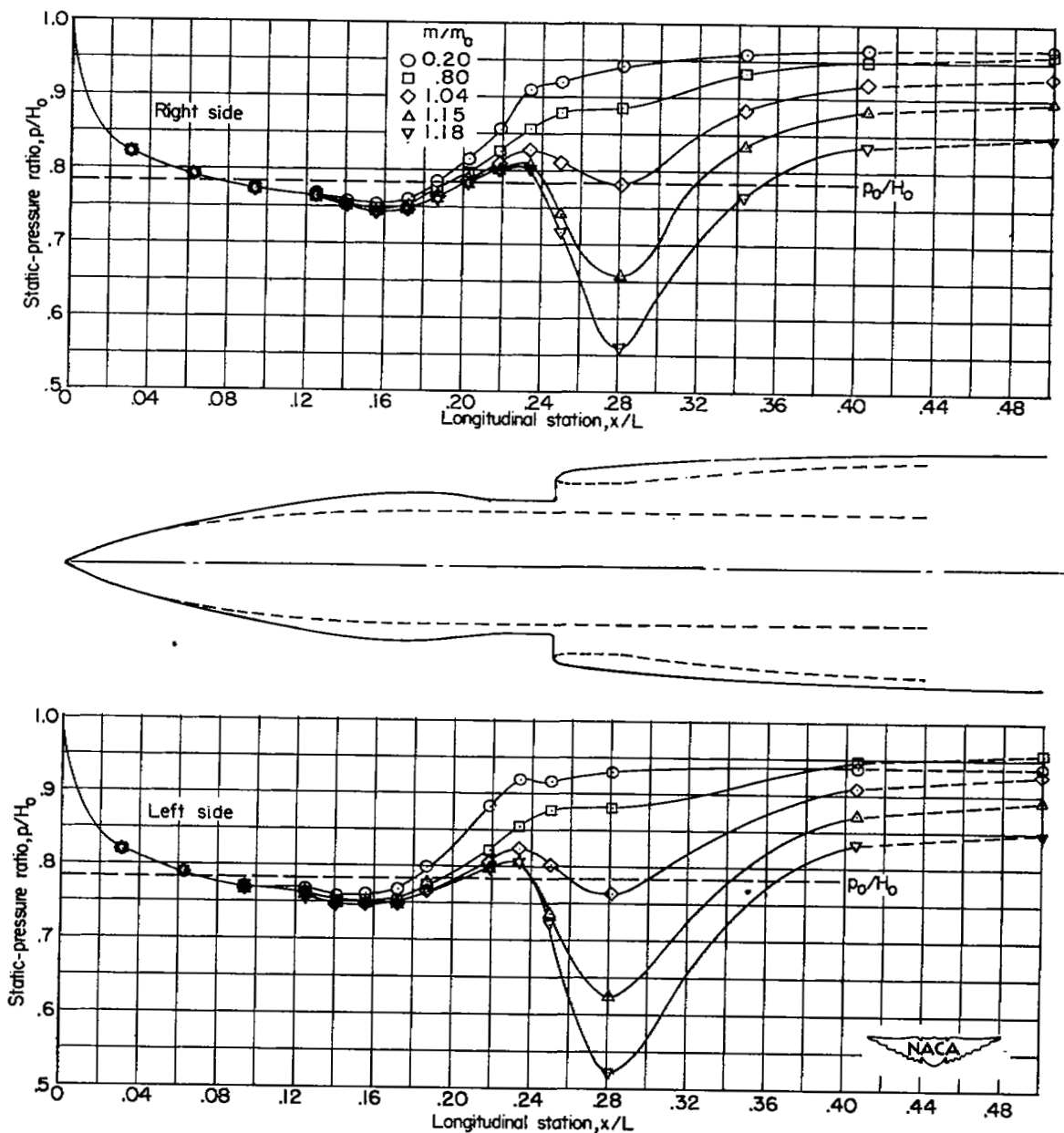
(a) $M_O = 0.60$.

Figure 7.- Comparison of static-pressure distributions at center line
of approach ramp for right- and left-hand ducts. $\alpha = 0°$.
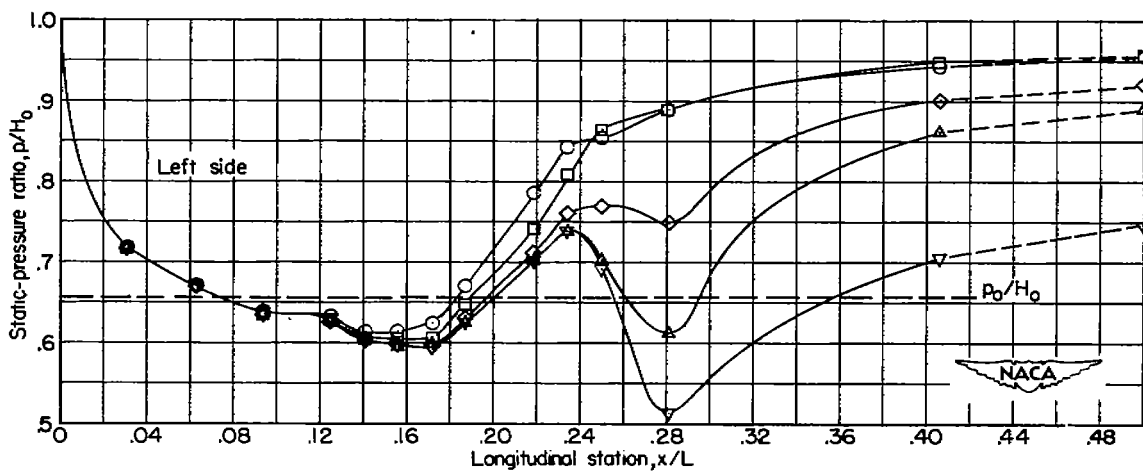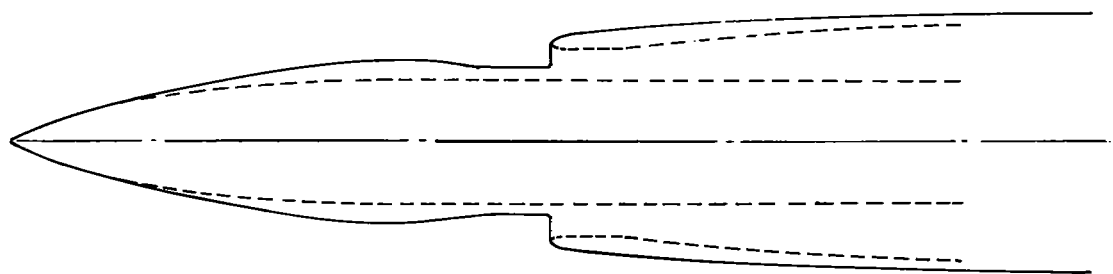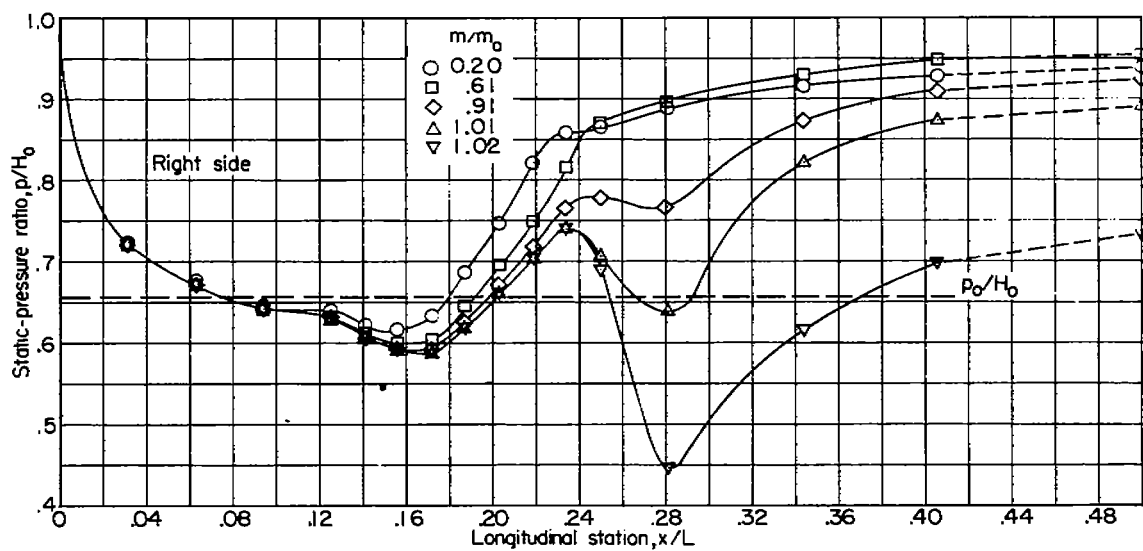
(b) $M_O = 0.80$.

Figure 7.- Continued.
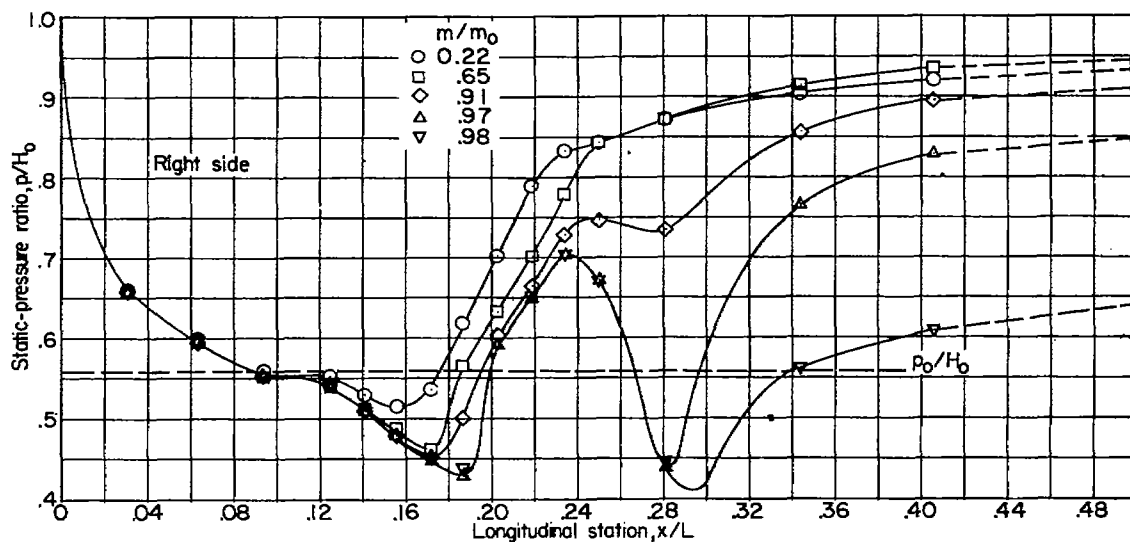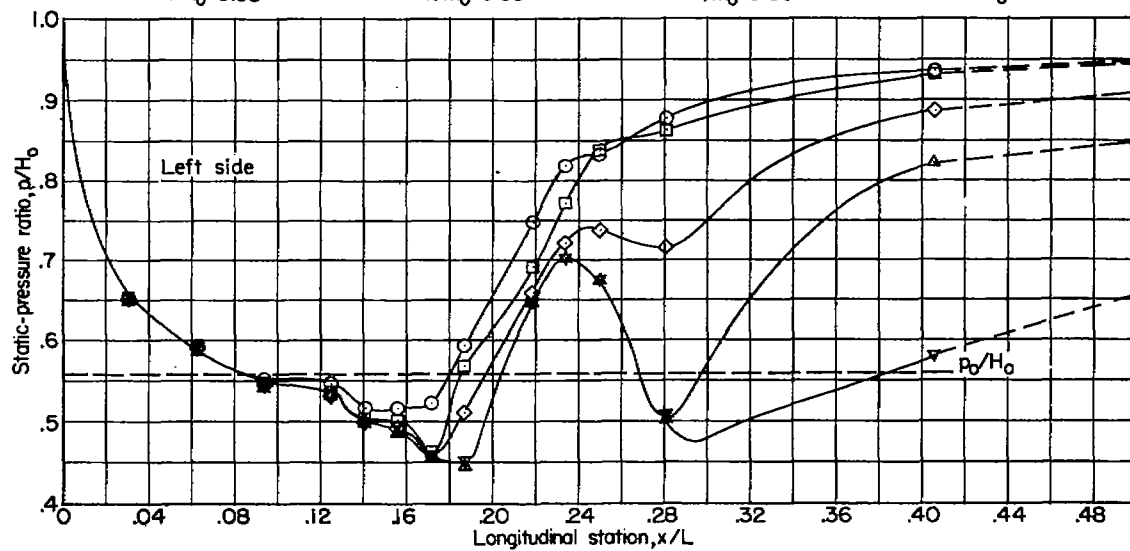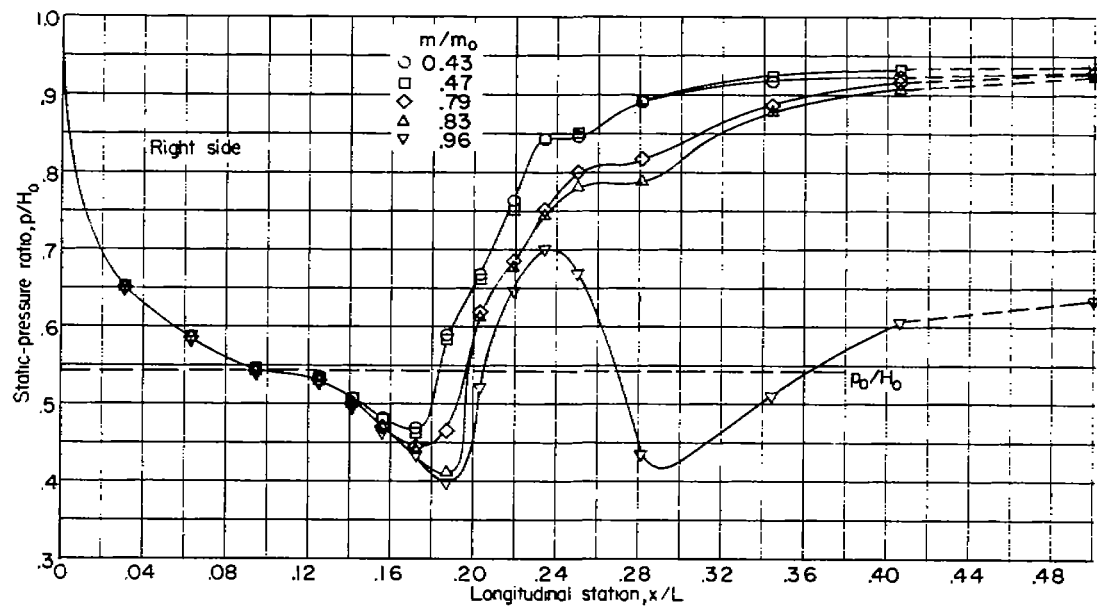
(c) $M_O = 0.95$.

Figure 7.- Continued.

L-77964

(d) $M_O = 0.975$.

Figure 7.- Continued.

(e) $M_O = 1.00$.
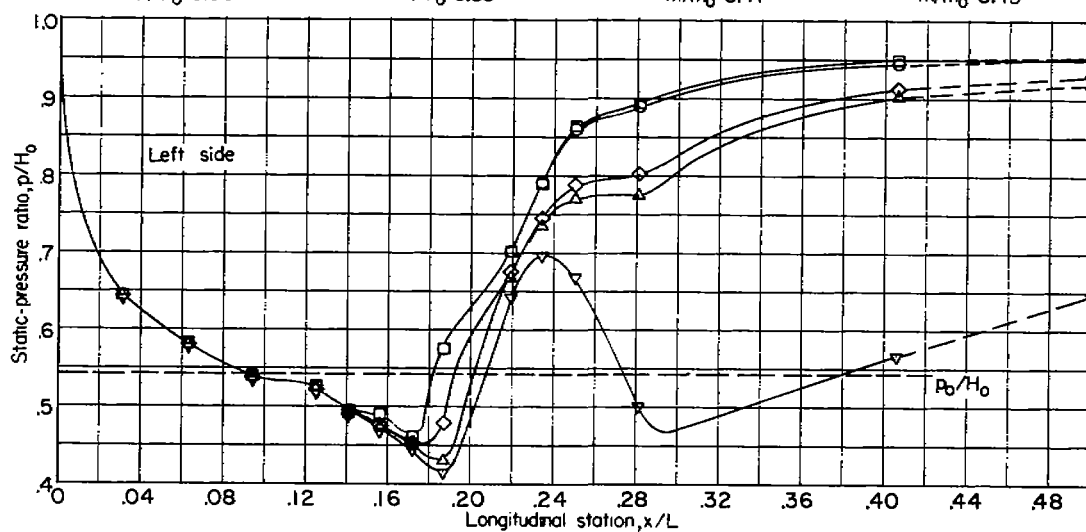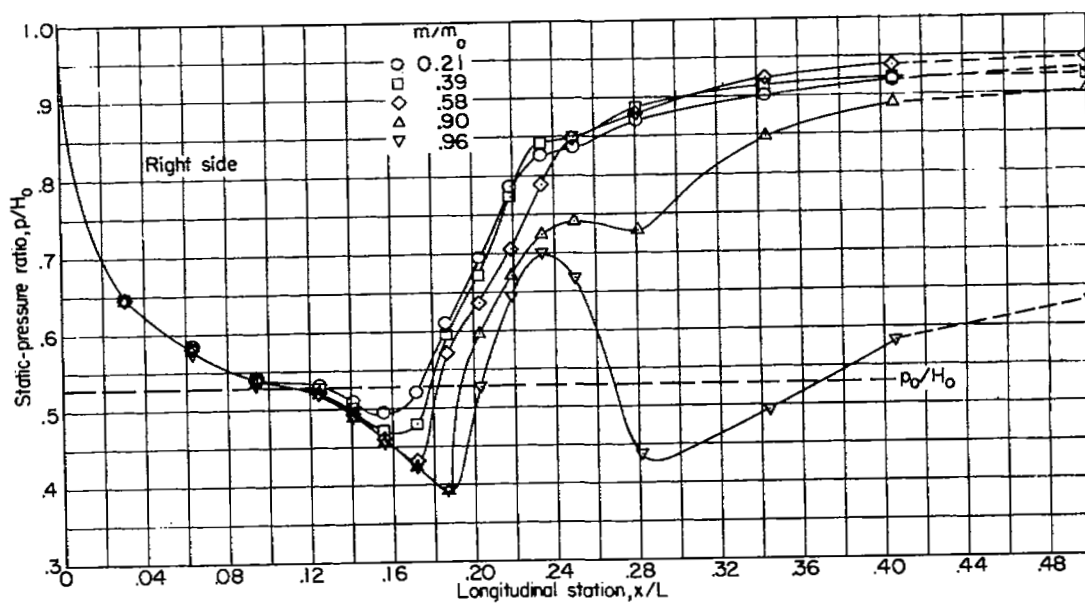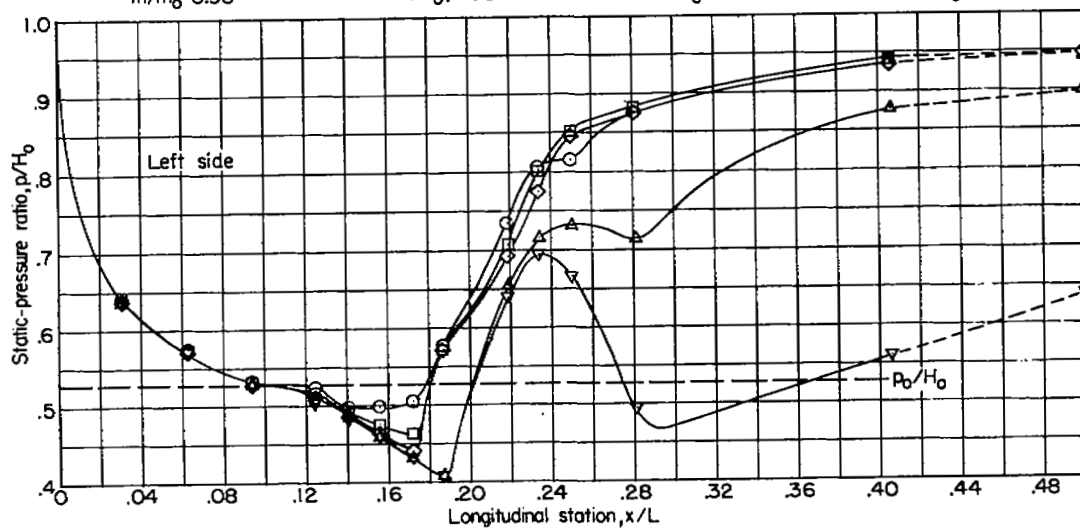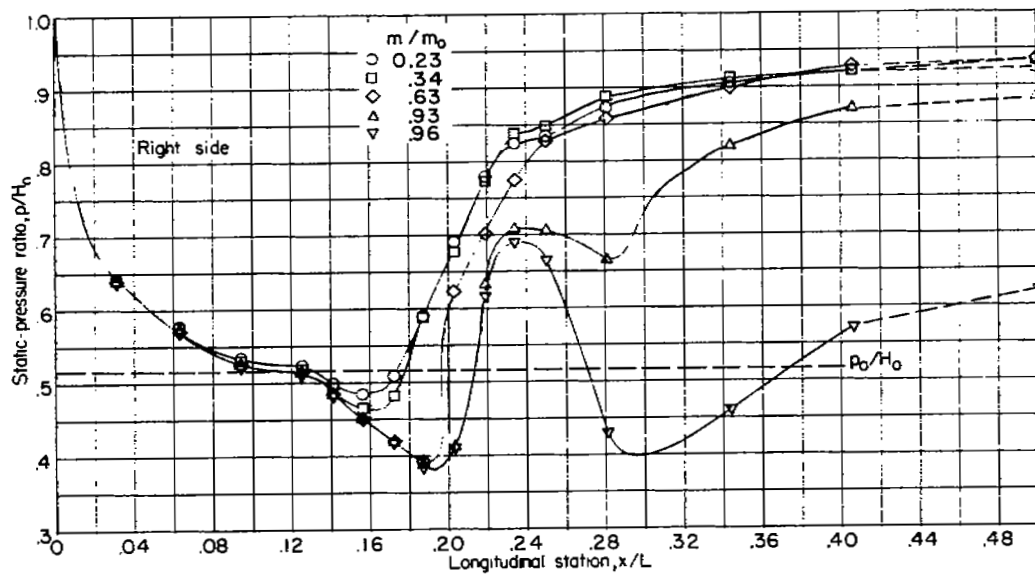
Figure 7.- Continued.
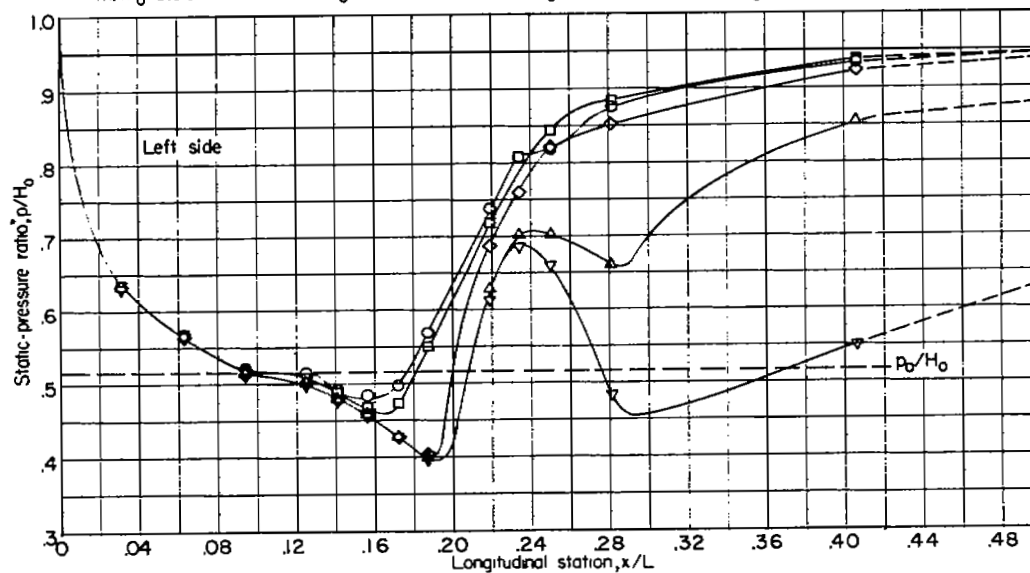
L-77966

(f) $M_O = 1.02$.

Figure 7.- Continued.

L-77967

(g) $M_O \approx 1.04$.
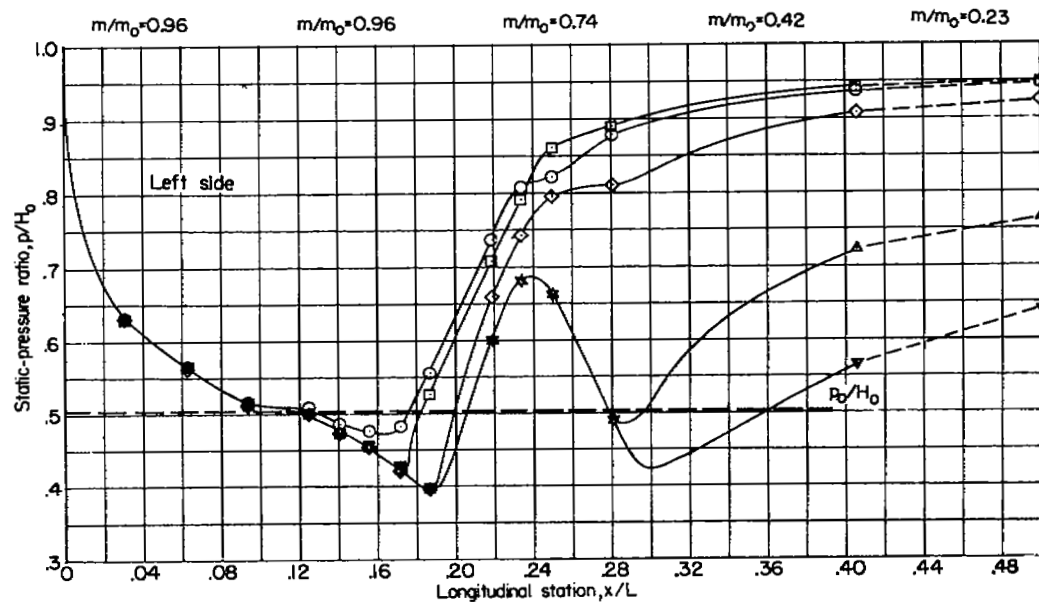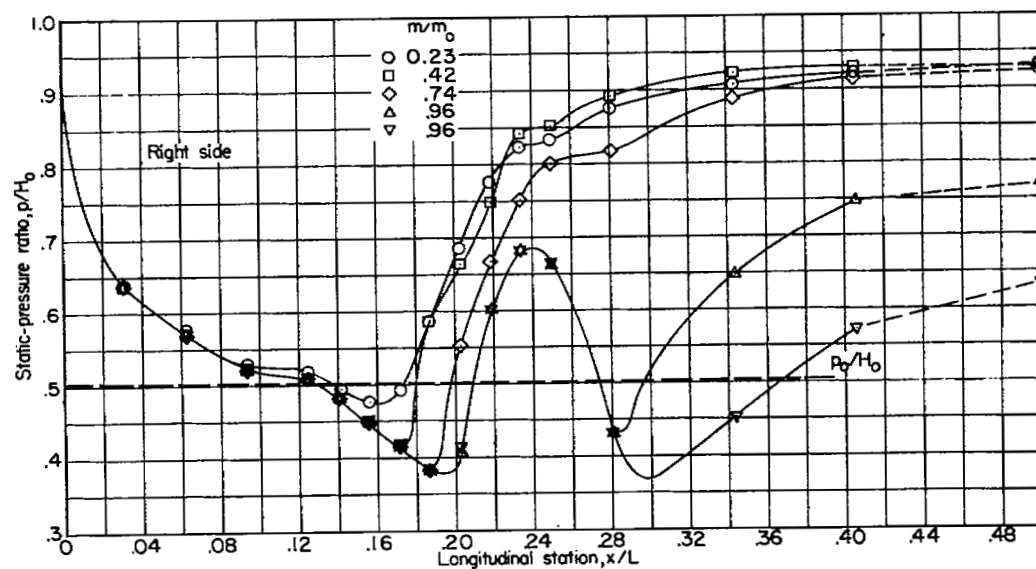
Figure 7.- Continued.
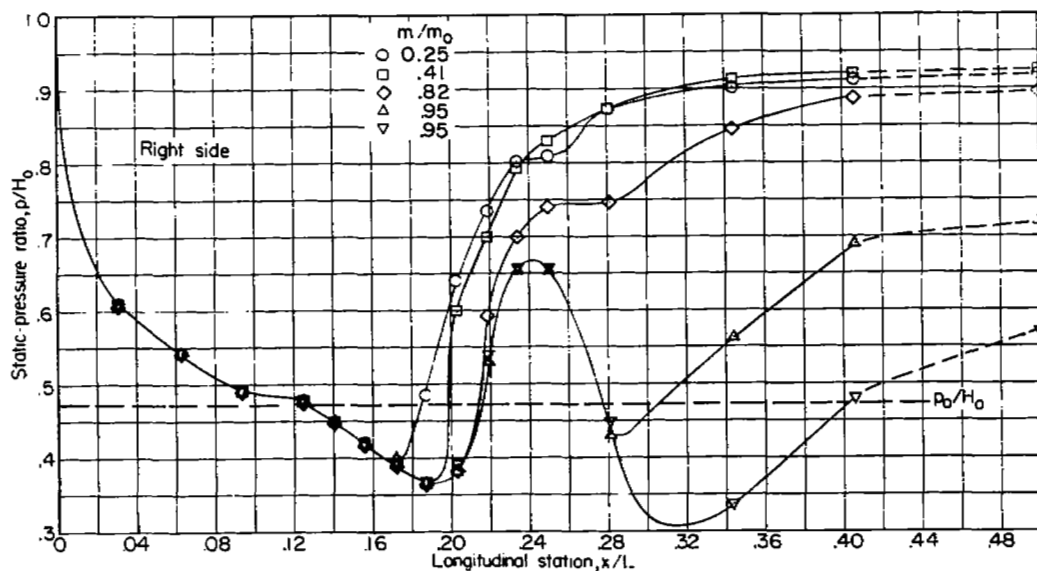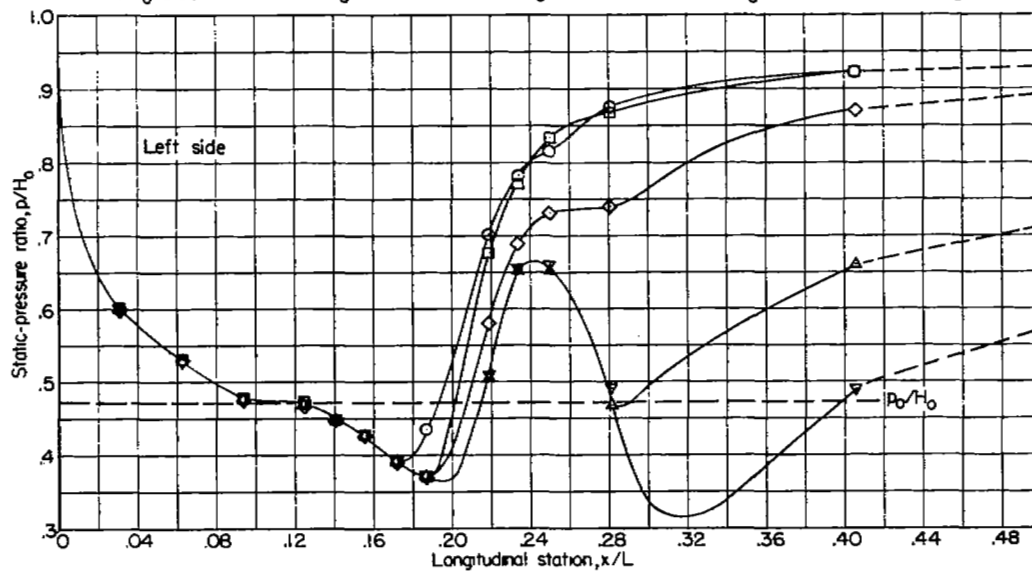
L-77968

(h) $M_0 \approx 1.09$.

Figure 7.- Concluded.

L-77969
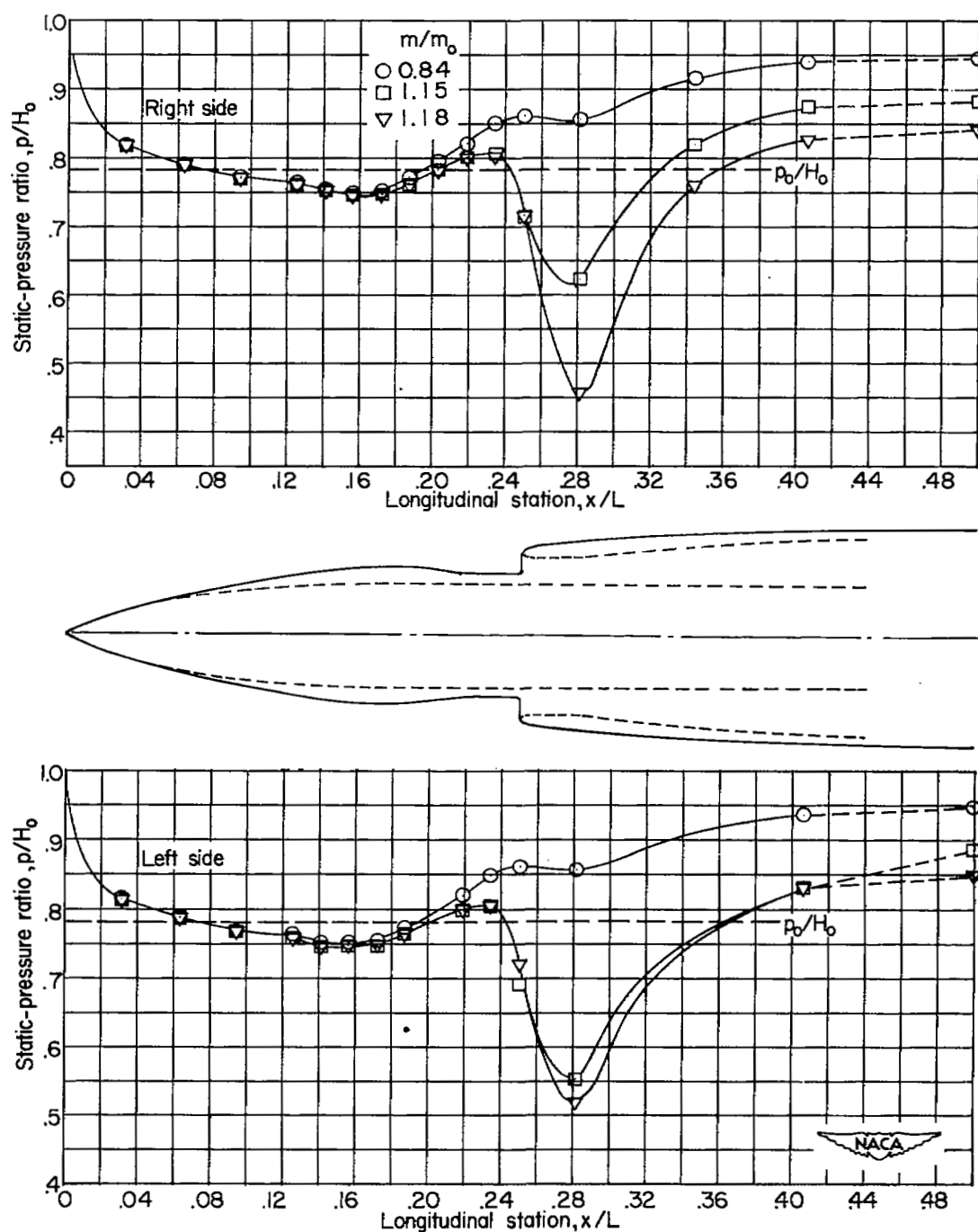
(a) $M_O = 0.60$.

Figure 8.- Variation of static pressure on both right- and left-hand
ramp center lines. $\alpha \approx 4.3^o$.
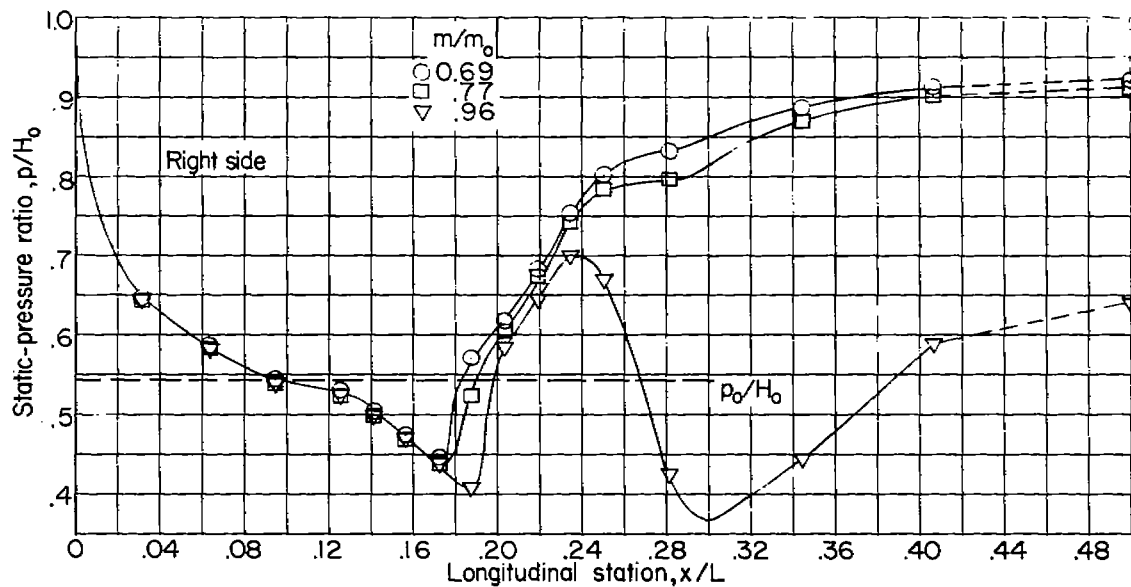
m/m₀=0.96   m/m₀=0.94   m/m₀=0.77   m/m₀=0.21
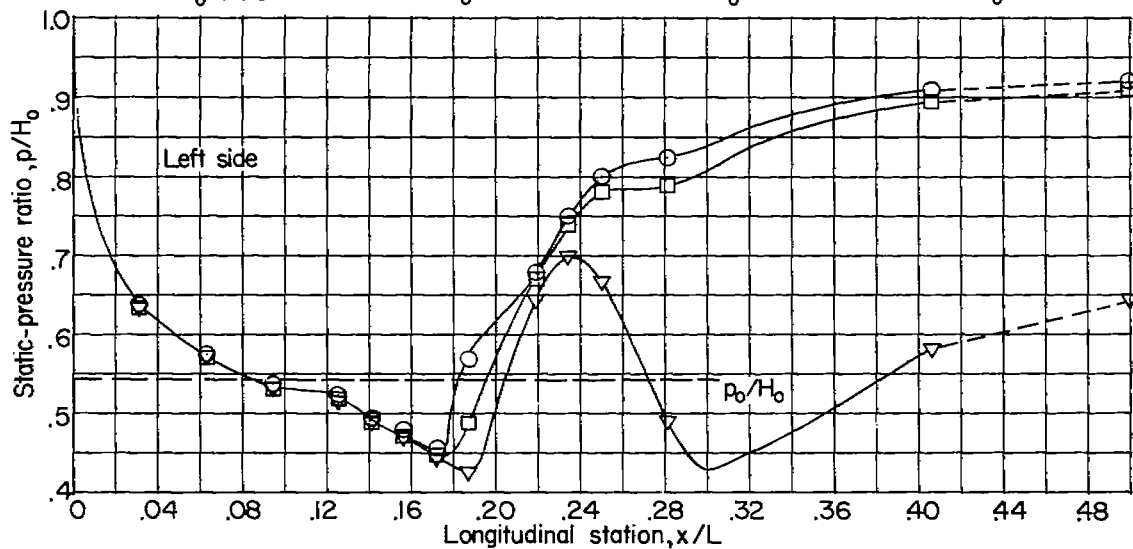
(b)   M₀ = 0.975.

Figure 8.- Continued.
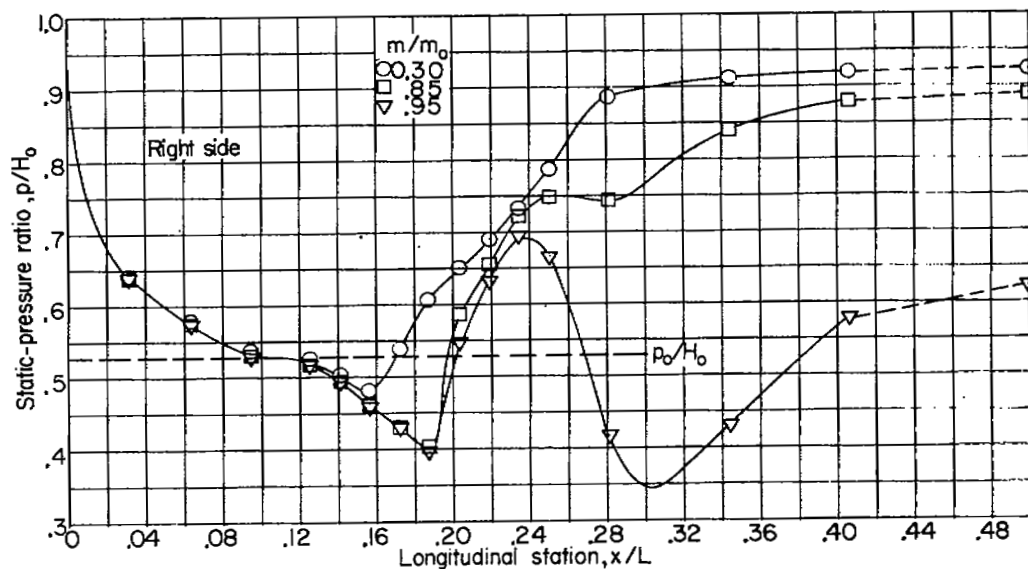
L-79177

(c) $M_O = 1.00$.
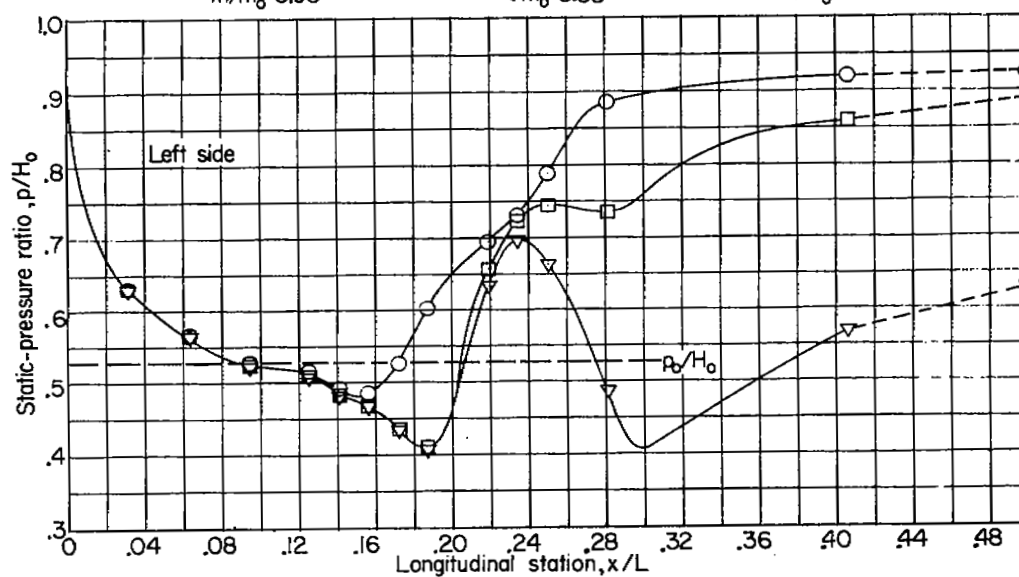
Figure 8.- Continued.
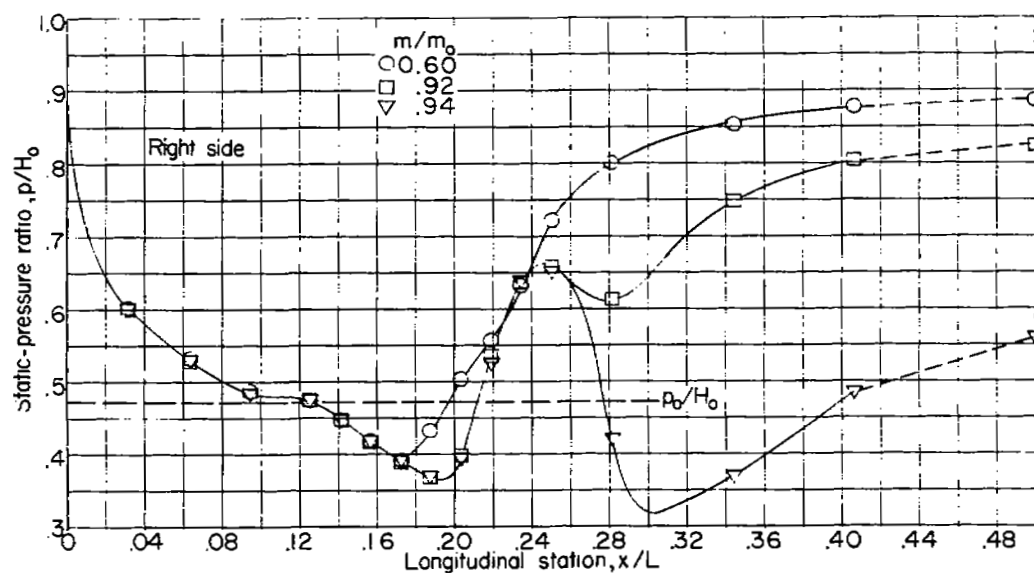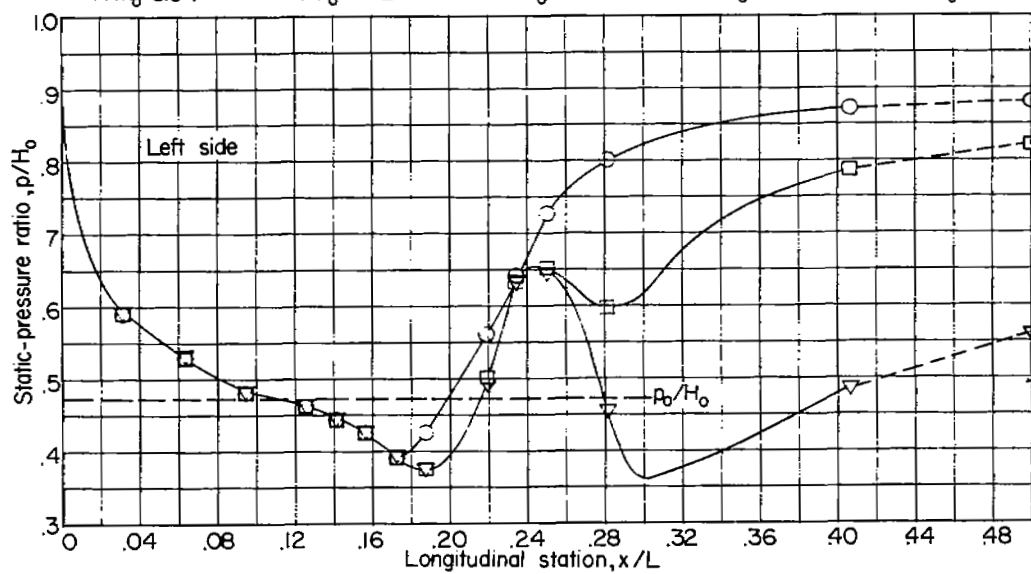
L-79178

(d) $M_O \approx 1.09$.
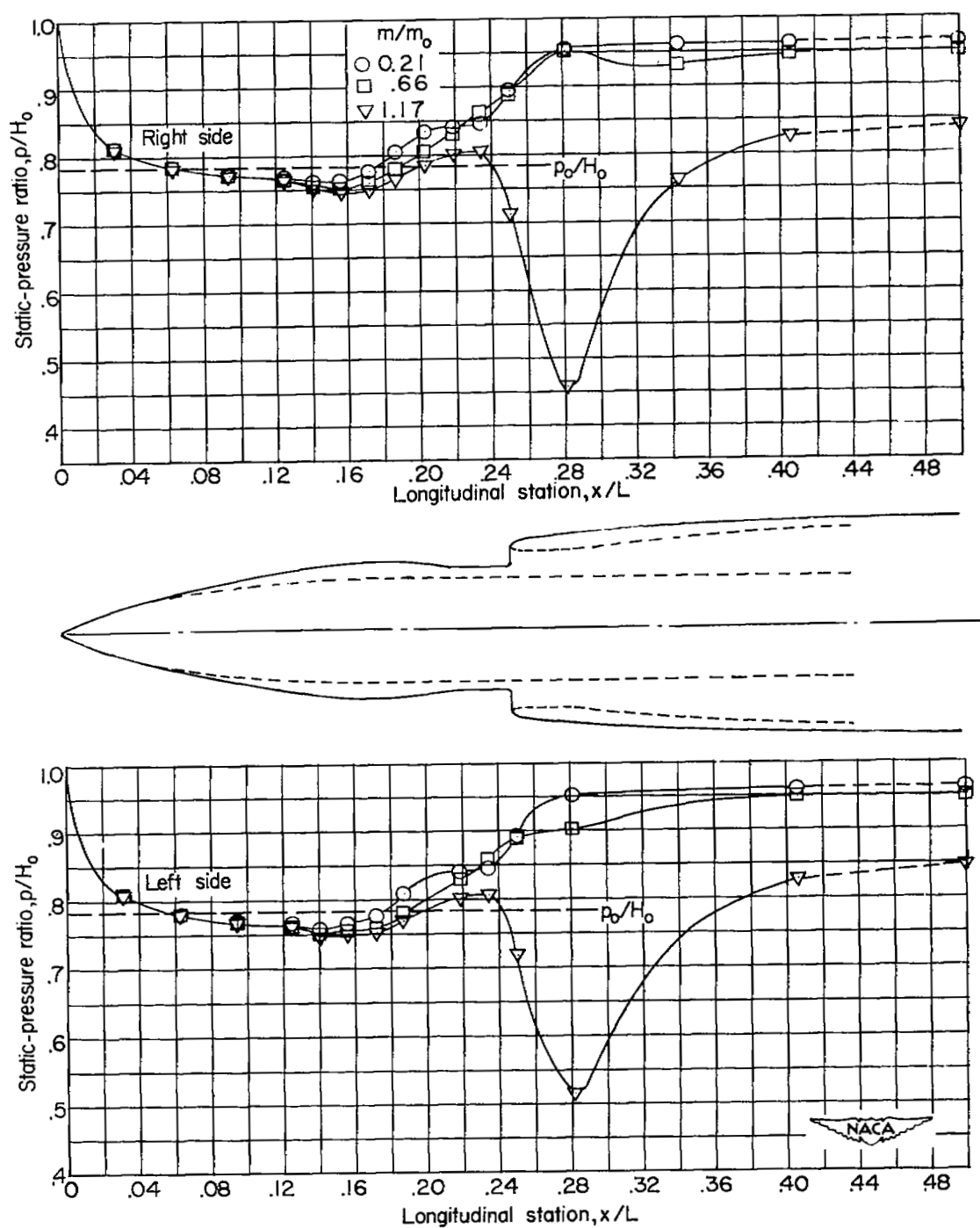
Figure 8.- Concluded.

(a) $M_O = 0.60$.

Figure 9.- Variation of static pressure at ramp center line. $\alpha \approx 7.3^{\circ}$.
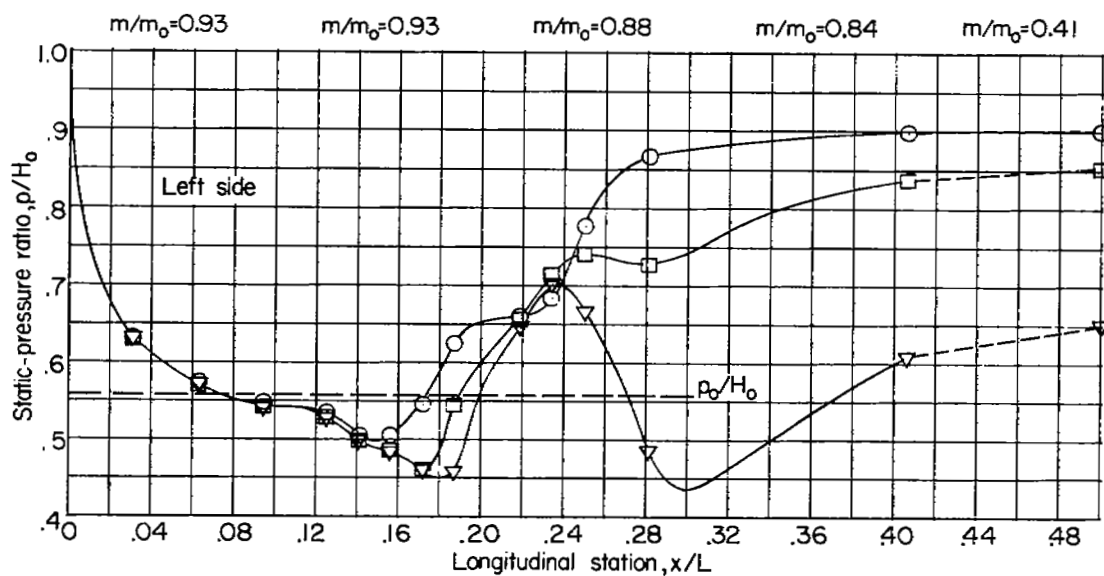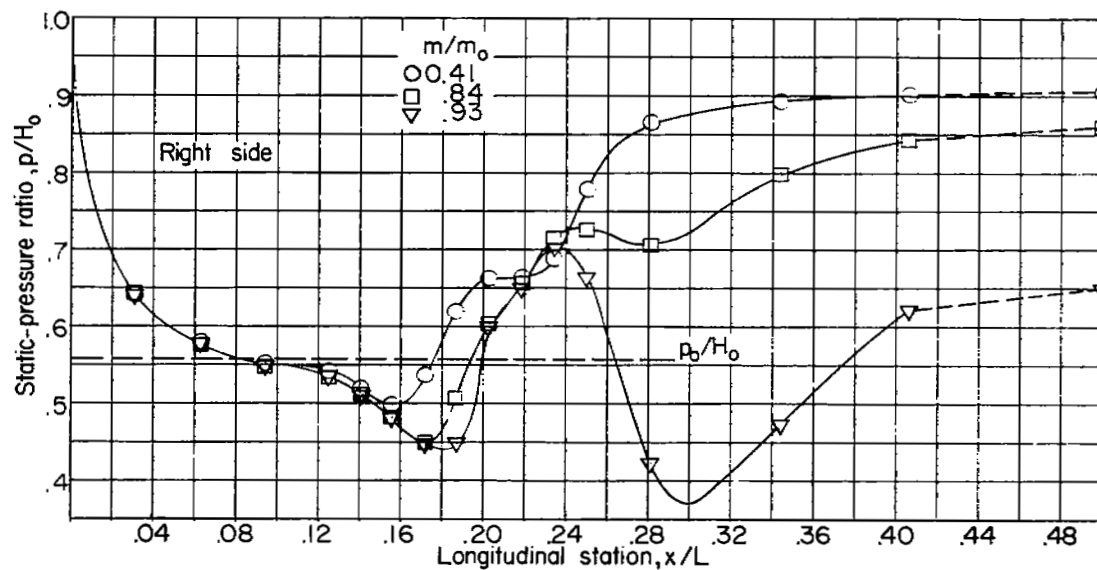
(b) M_O = 0.95.

Figure 9.- Continued.

L-79180
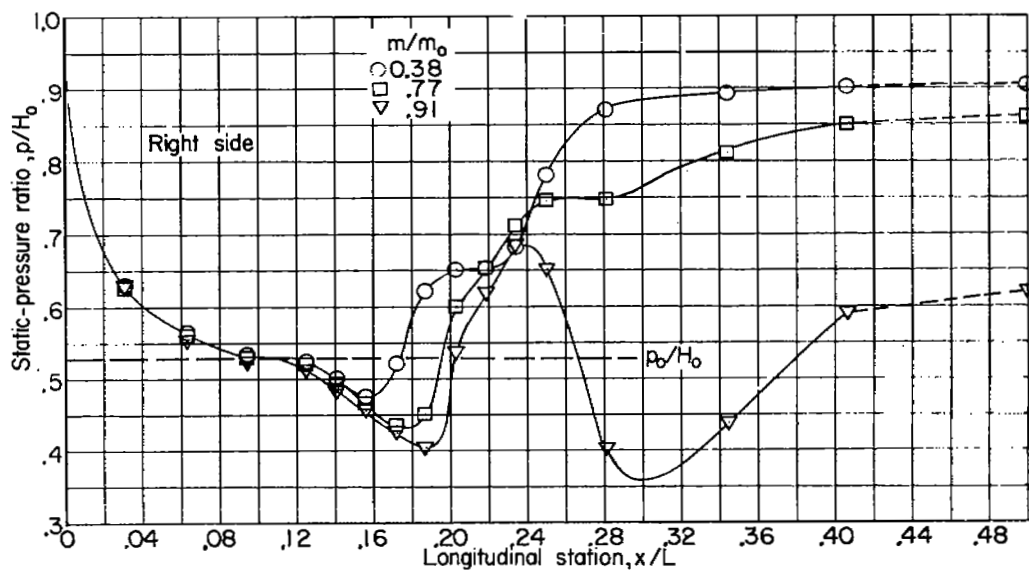
(c) $M_O = 1.00$.
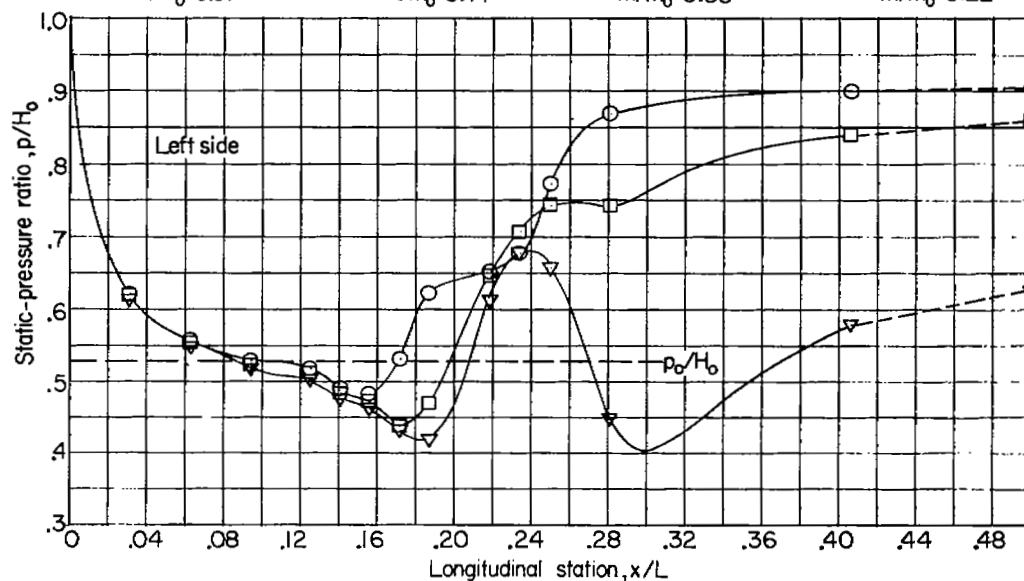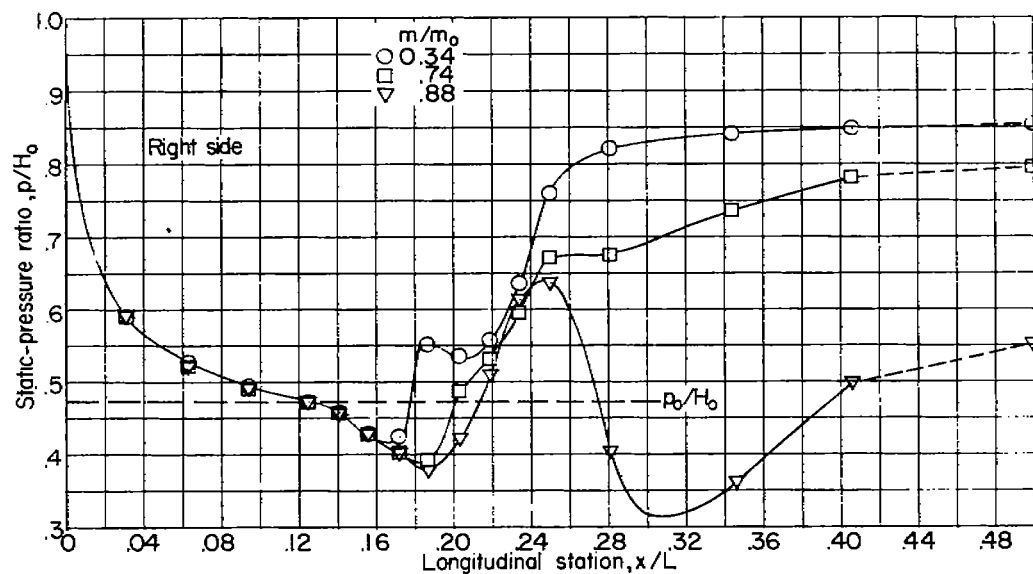
Figure 9.- Continued.
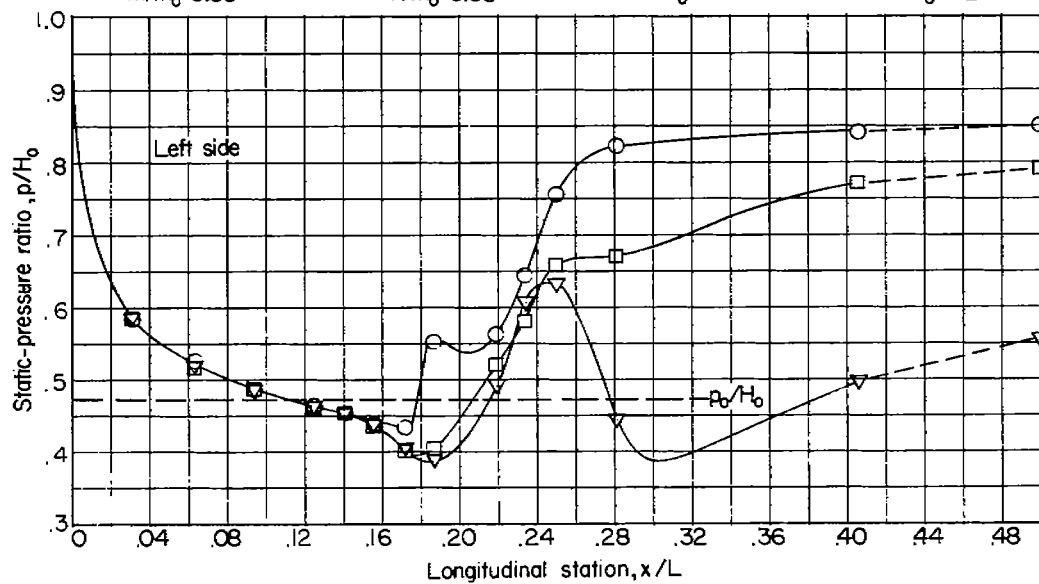
L-79181

(d) $M_0 \approx 1.09.$

Figure 9.- Concluded.

L-79182
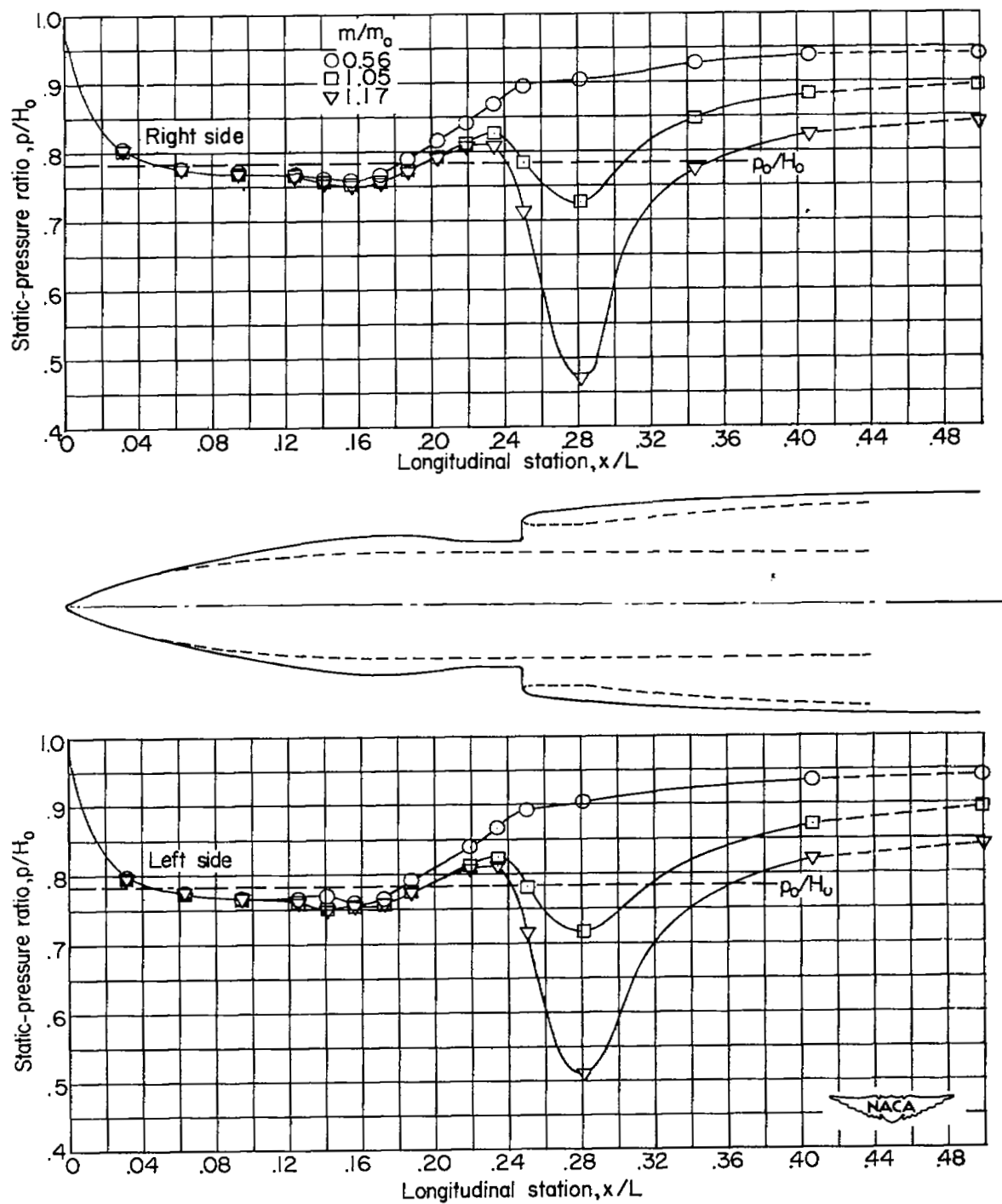
(a) $M_O = 0.60$.

Figure 10.- Variation of static pressure along ramp center line. $\alpha \approx 10.6^O$.
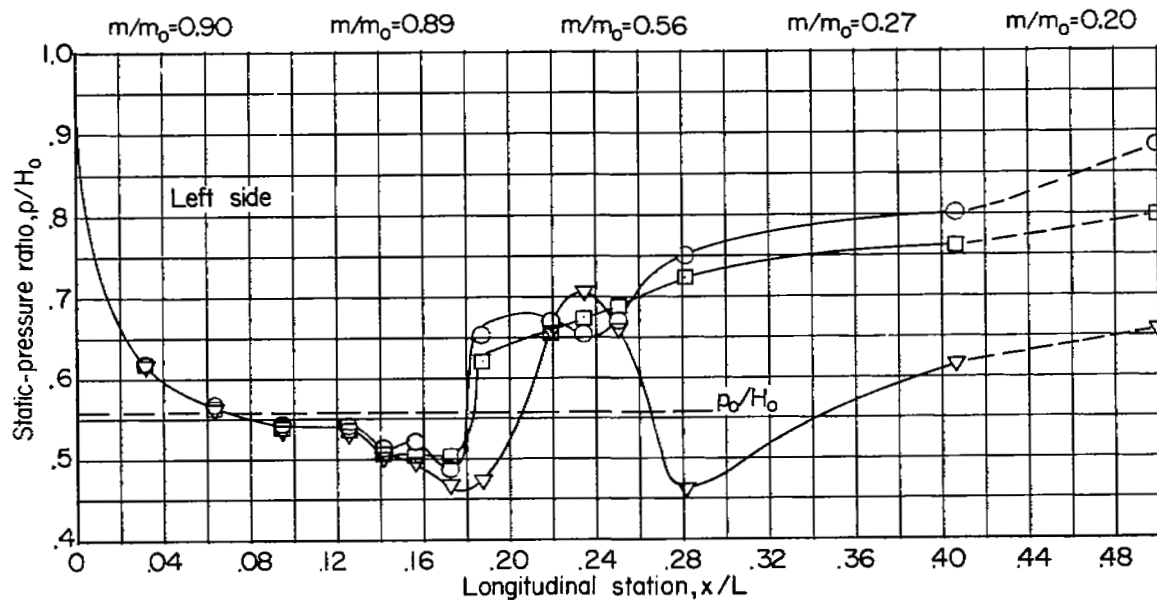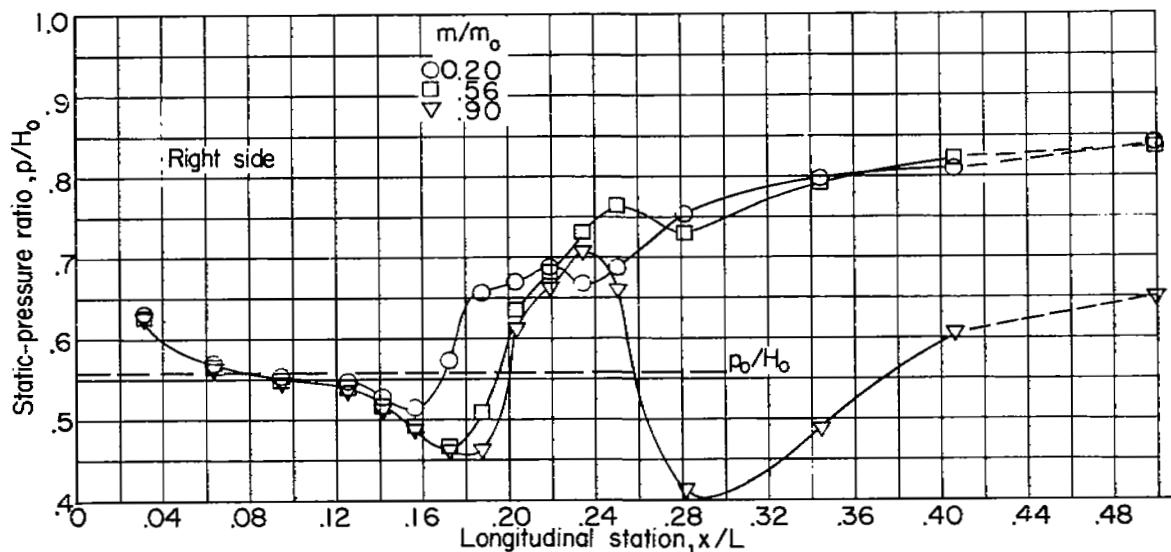
(b) M_0 = 0.95.

Figure 10.- Continued.

L-79183

(c) $M_O = 1.00$.
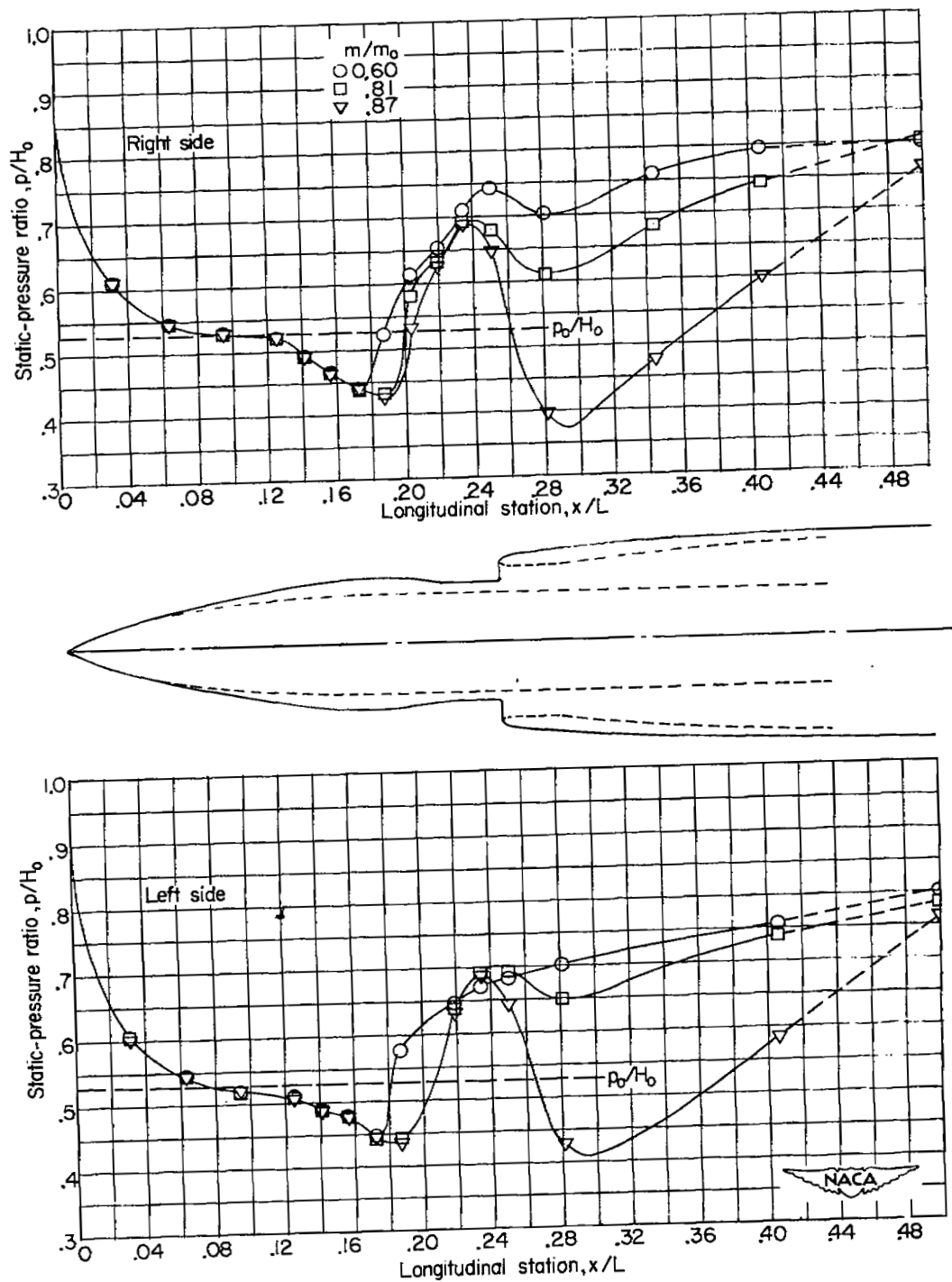
Figure 10.- Continued.
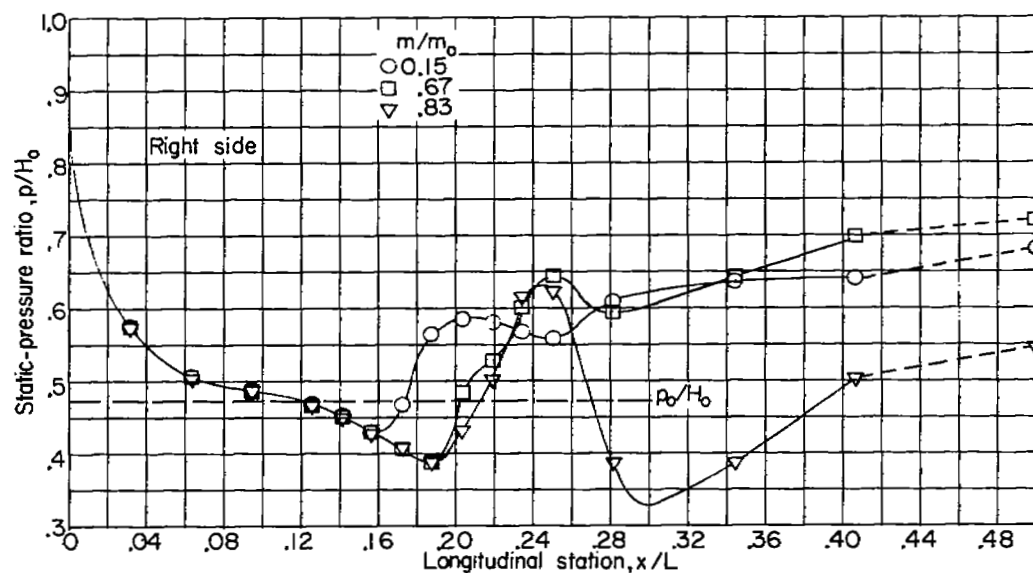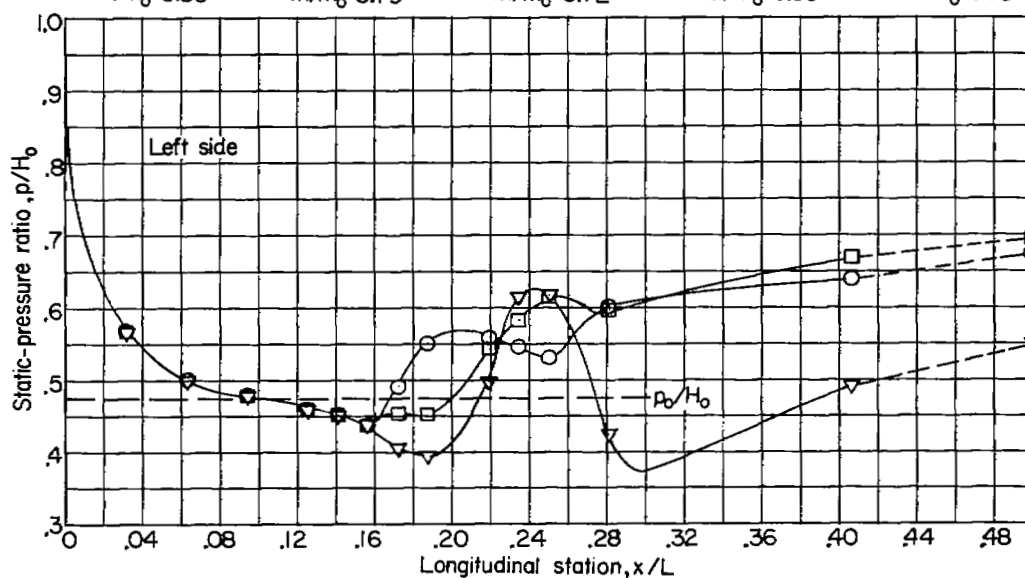
(d) $M_0 \approx 1.09$.

Figure 10.- Concluded.

L-79184

(a) $\alpha = 0°$.

(b) $\alpha \approx 10.6°$.
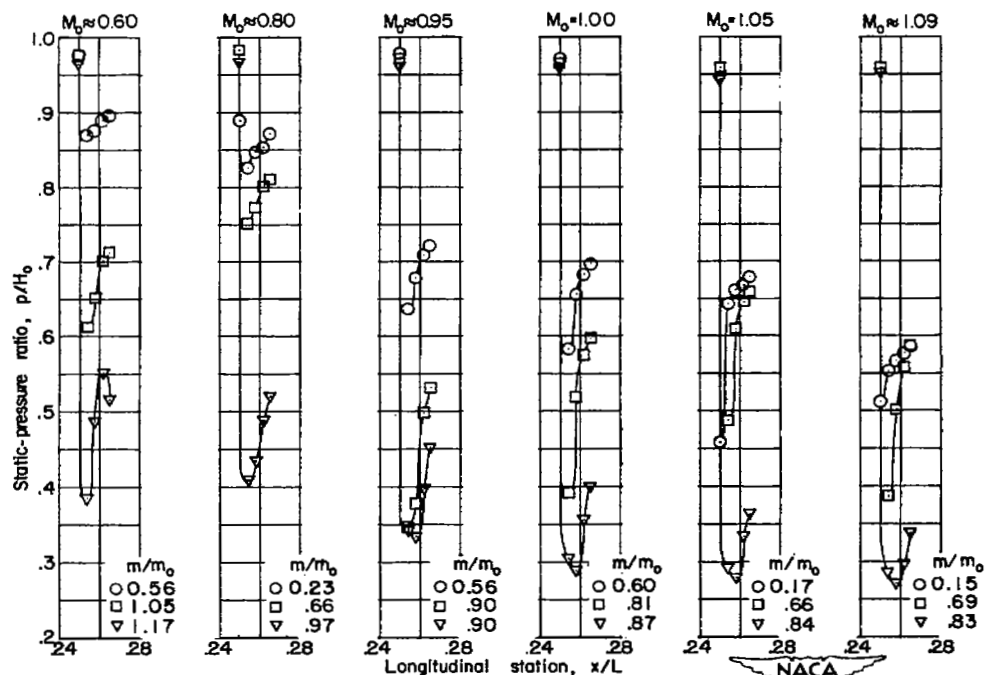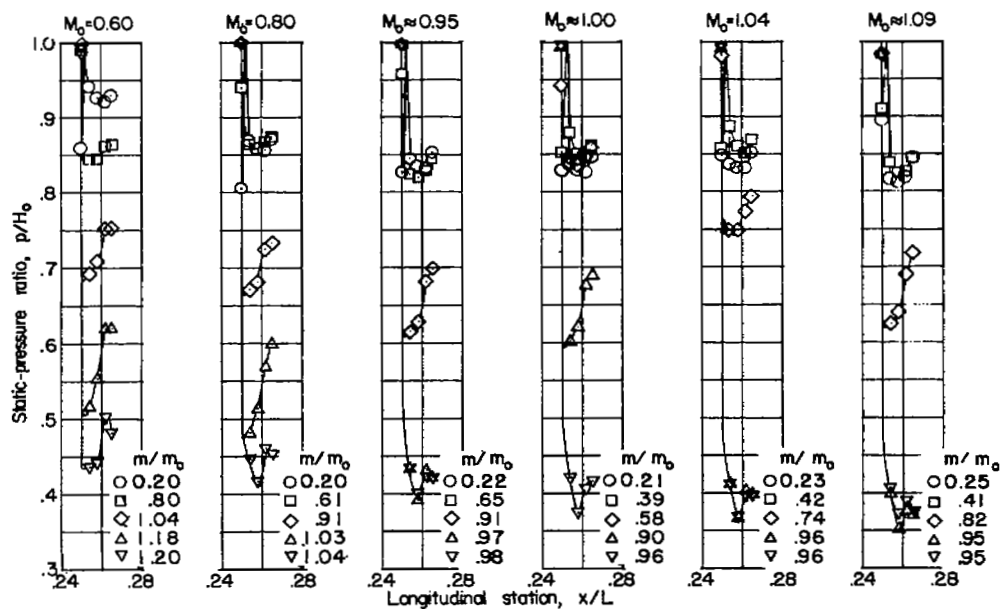
Figure 11.- Static-pressure distributions on inside of inlet lip.
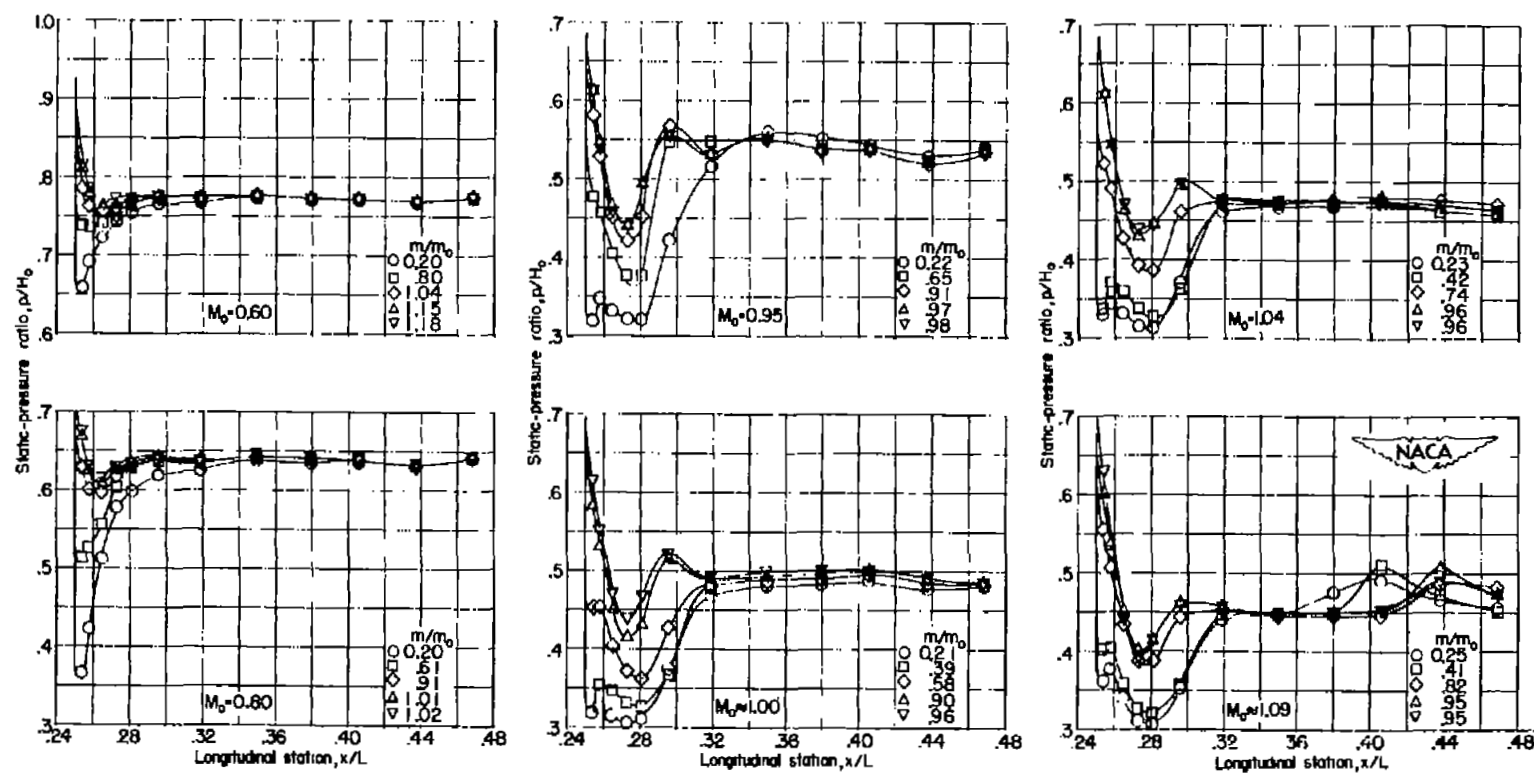
Figure 12.- Pressure distribution on exterior of lip along body center line. $\alpha = 0^{\circ}$.
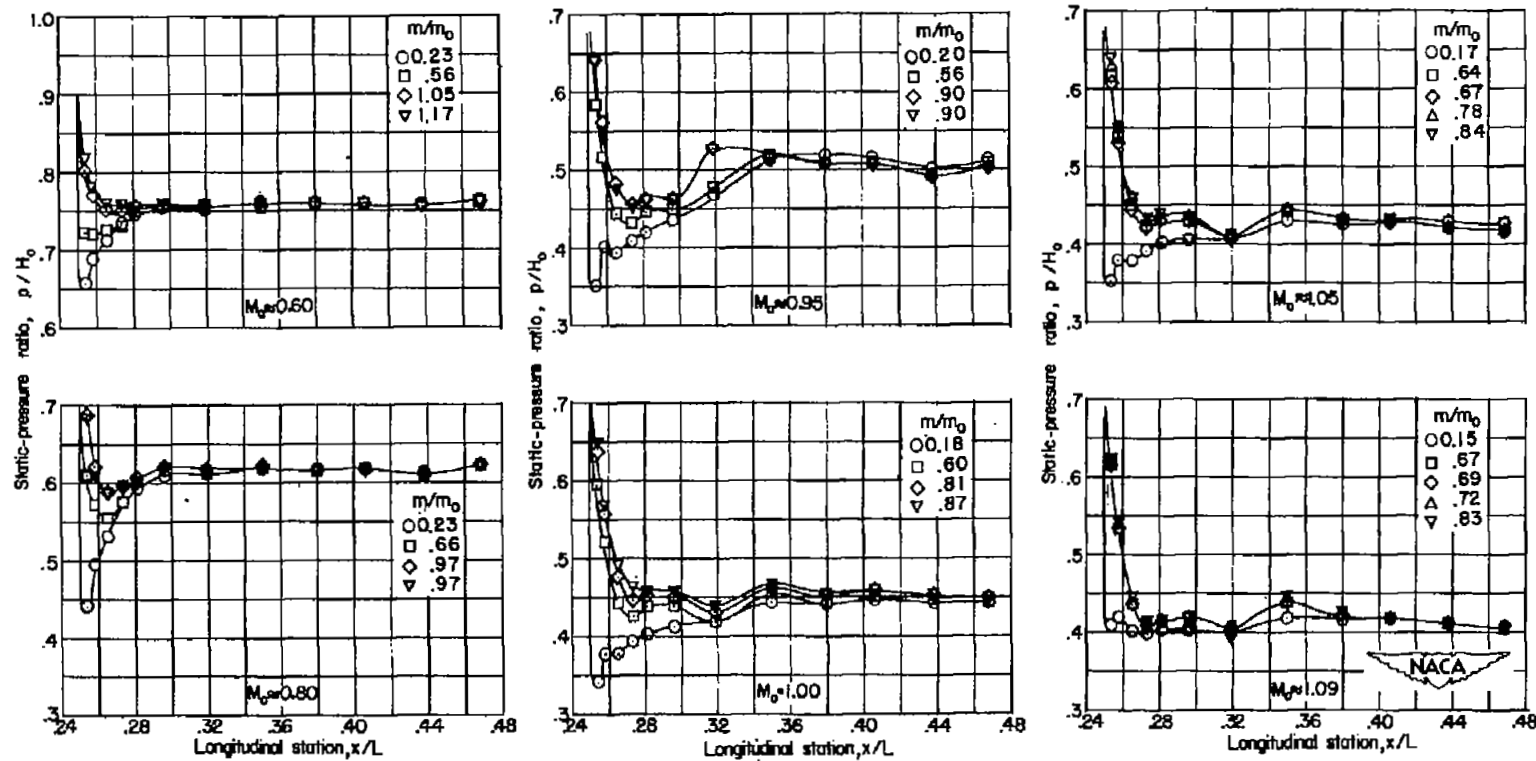
Figure 13.- Pressure distribution on exterior of lip along body center line. α ≈ 10.6°.
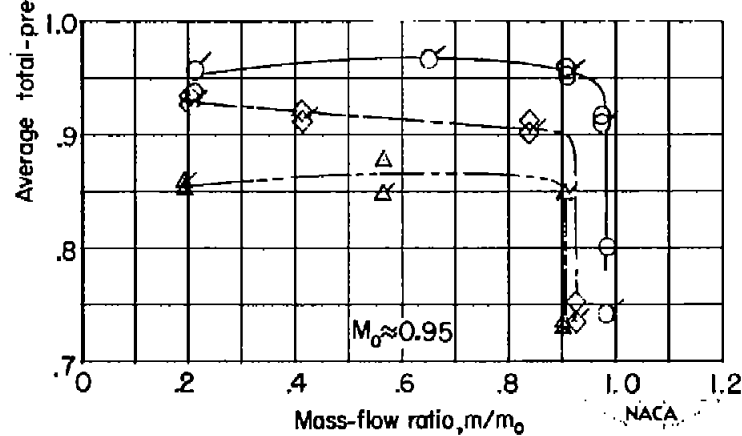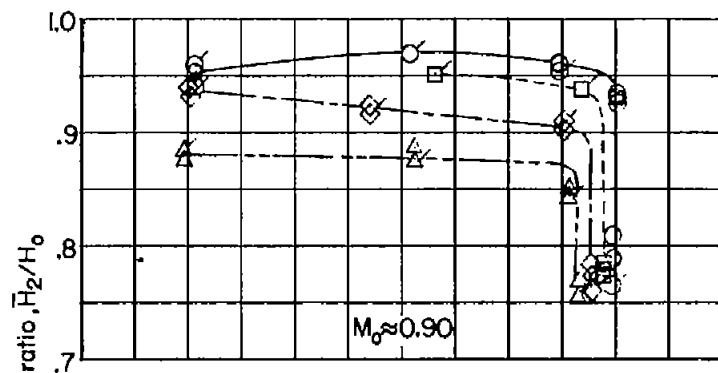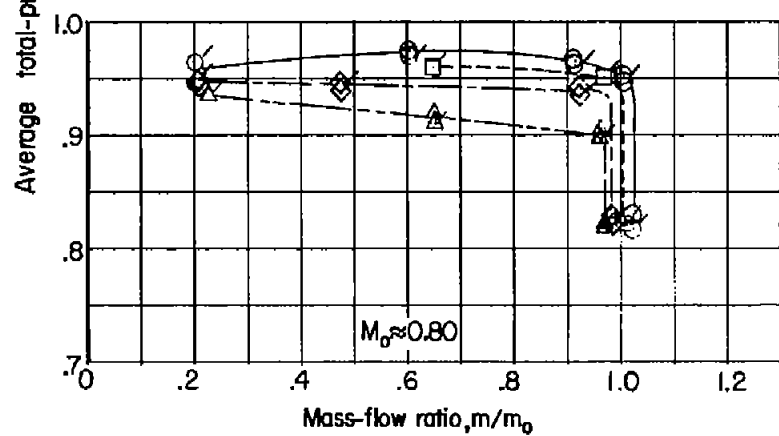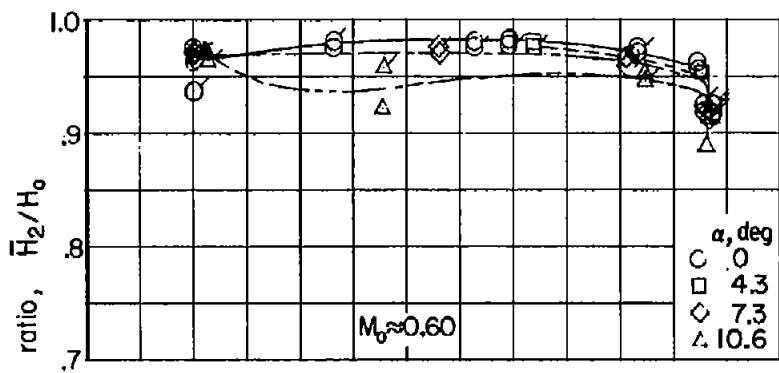
Figure 14.- Total-pressure-ratio characteristics of the submerged inlet at end of the diffuser. Flagged symbols indicate left duct.
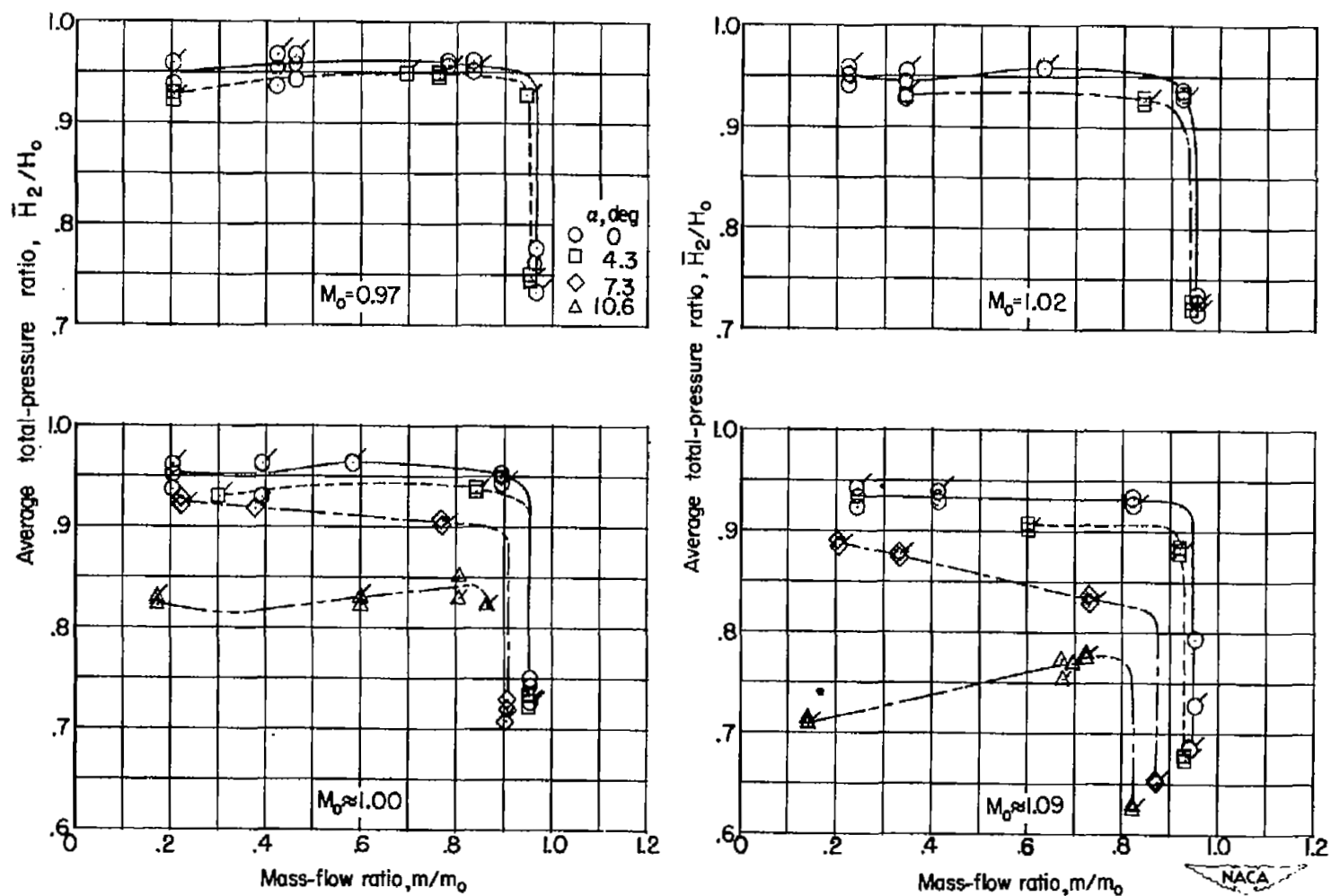
Figure 14.- Concluded.
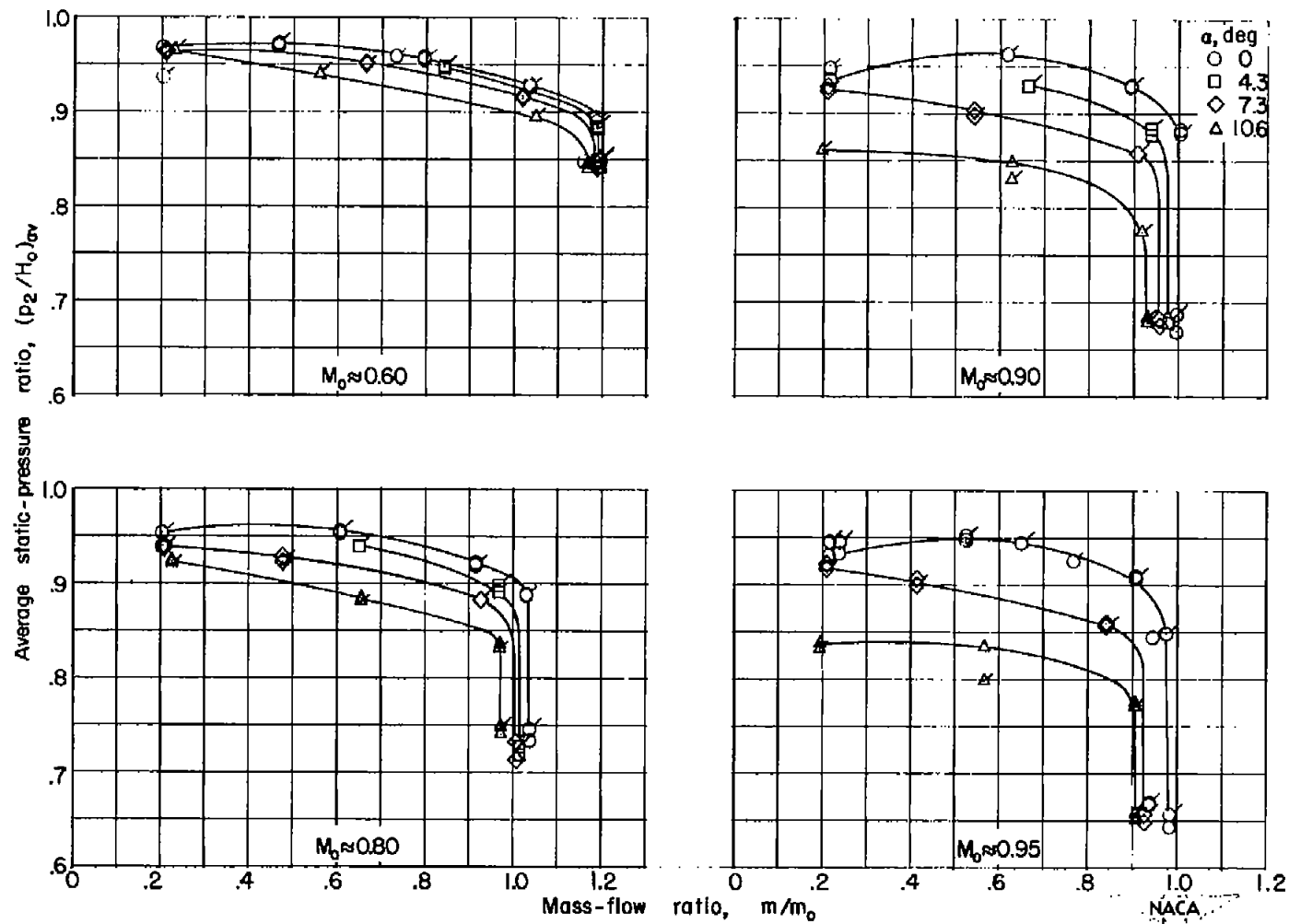
Figure 15.- Variation of the average static-pressure ratio at the end
of the diffuser for four test angles of attack. Flagged symbols
indicate left duct.
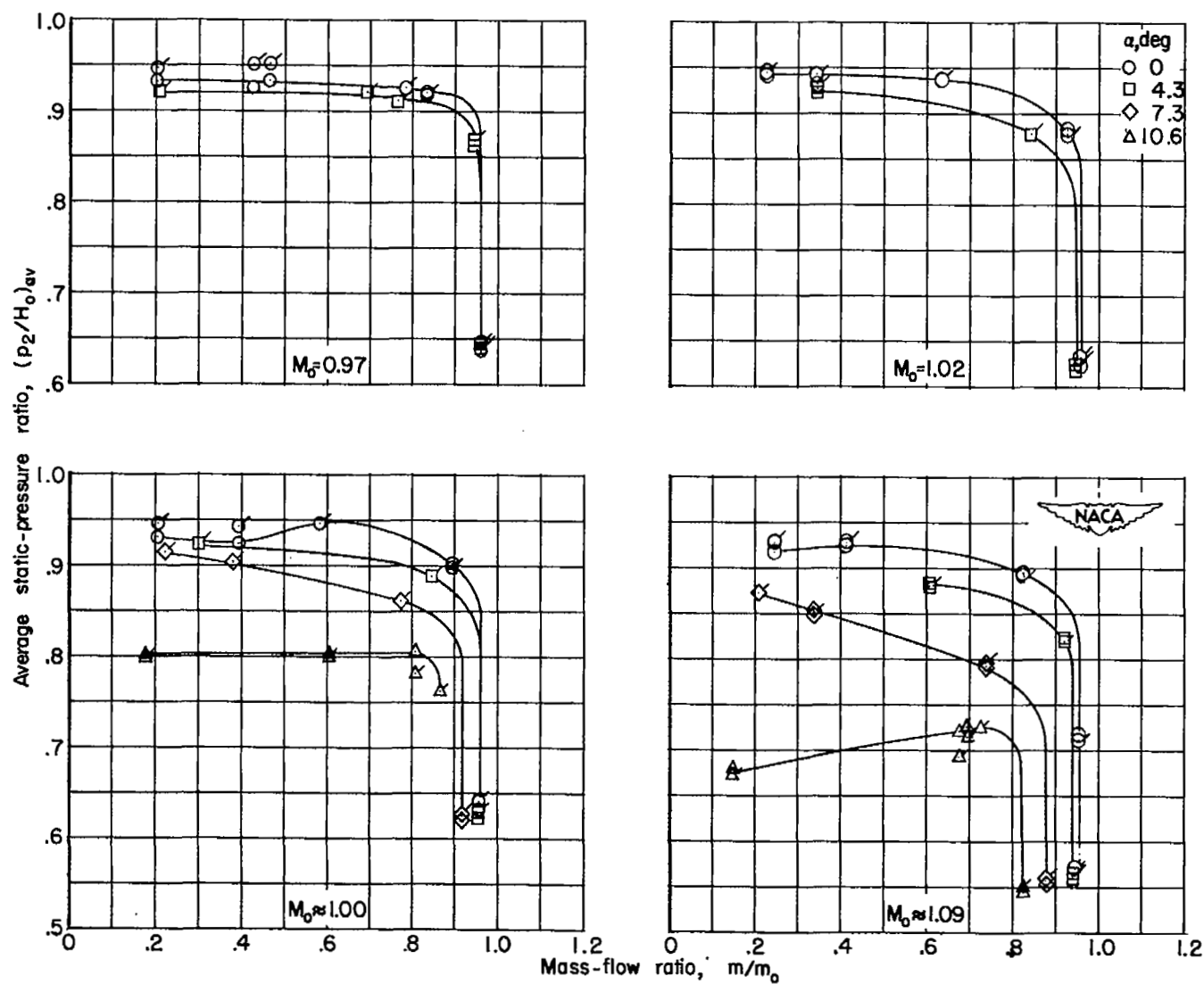
Figure 15.- Concluded.
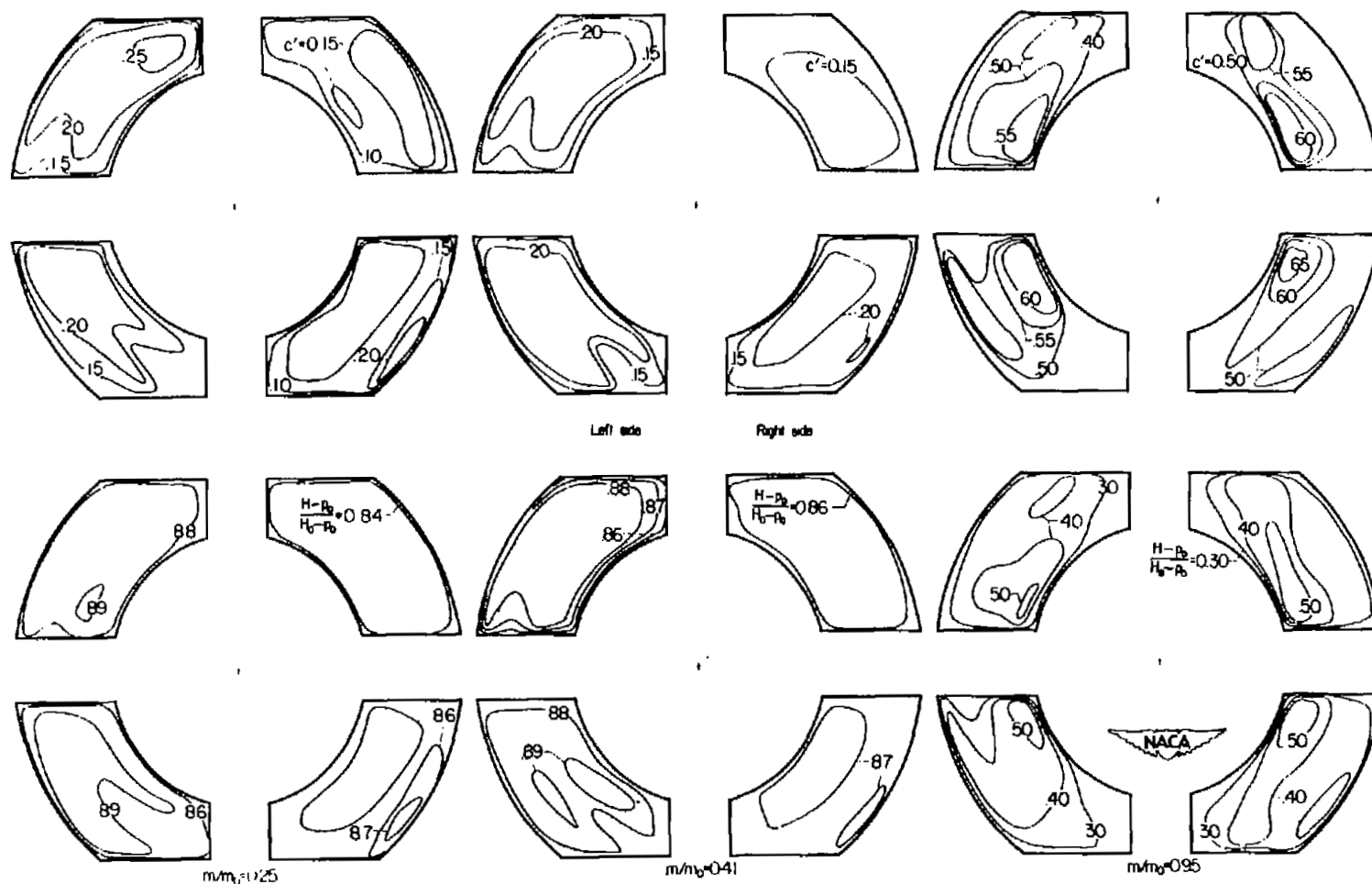
(a) $\alpha = 0^{\circ}$.

Figure 16.- Mass-flow-ratio and impact-pressure-ratio contours
after 2.4/1 diffusion. $M_0 \approx 1.09$.
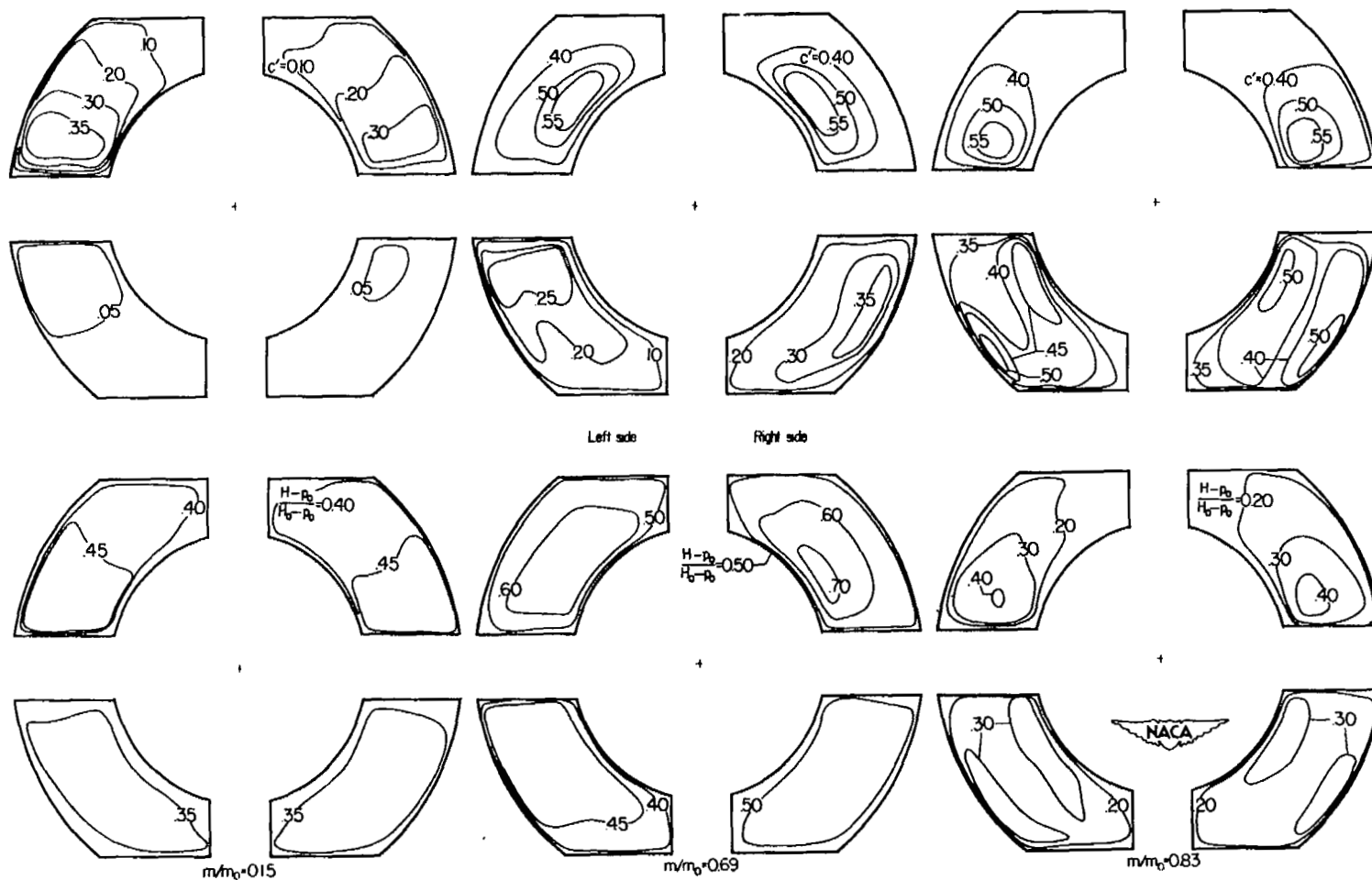
(b) α ≈ 10.6°.

Figure 16.- Concluded
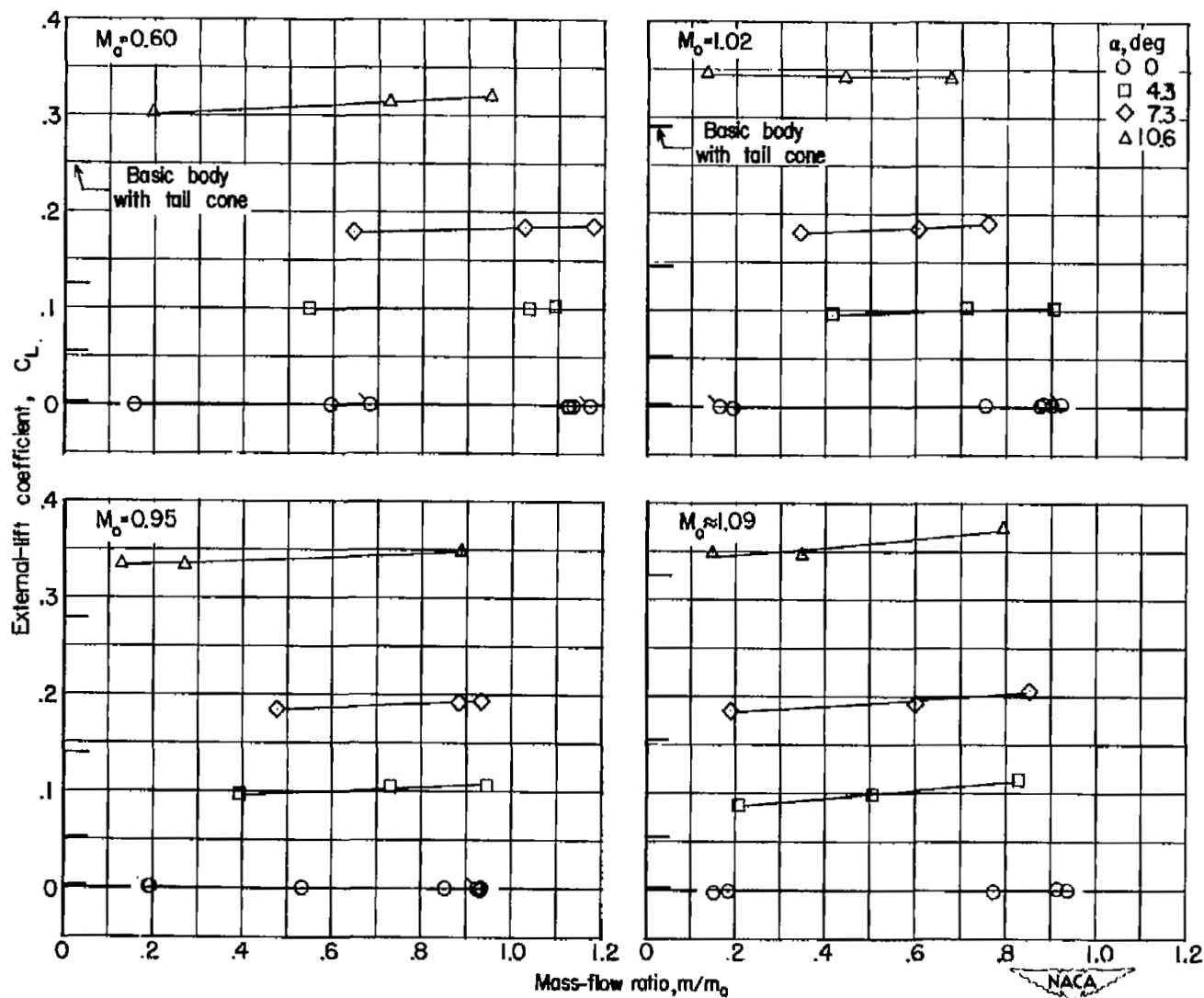
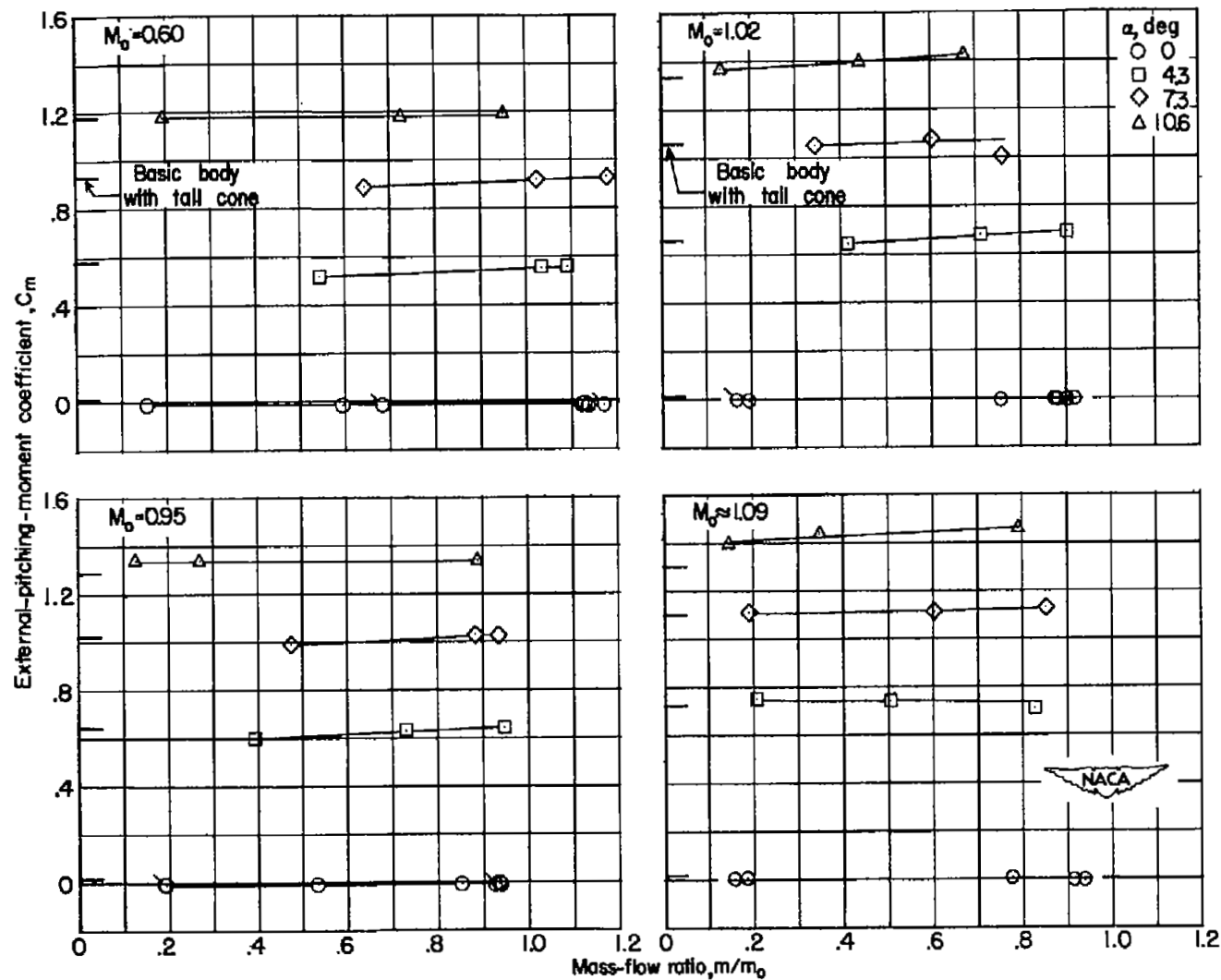Figure 17.- Effect of angle of attack and mass-flow ratio on external lift coefficient.

Figure 18.- Variation of external pitching moment with mass-flow ratio for several angles of attack.
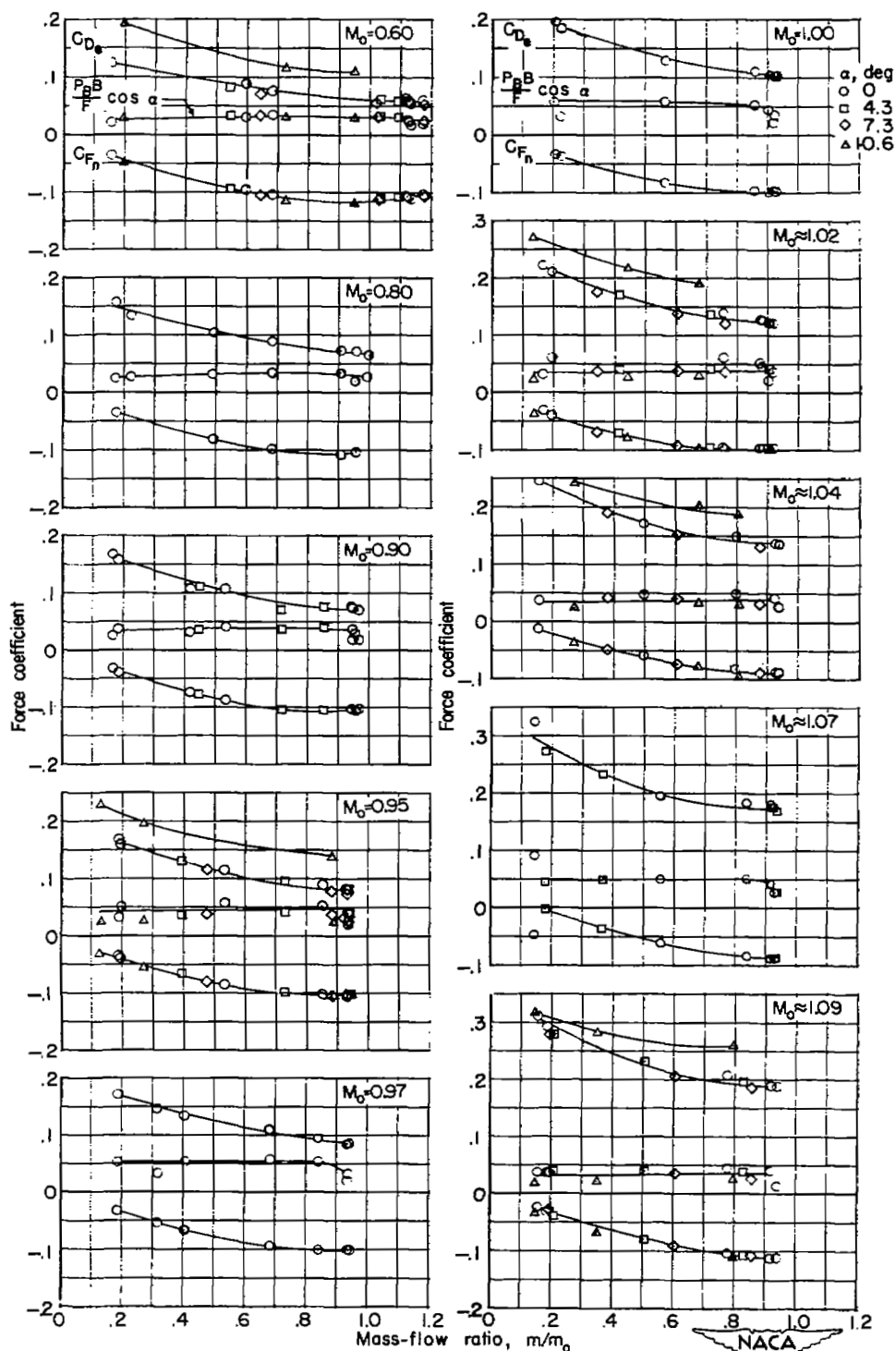
Figure 19.- Variation of dragwise forces with mass-flow ratio for
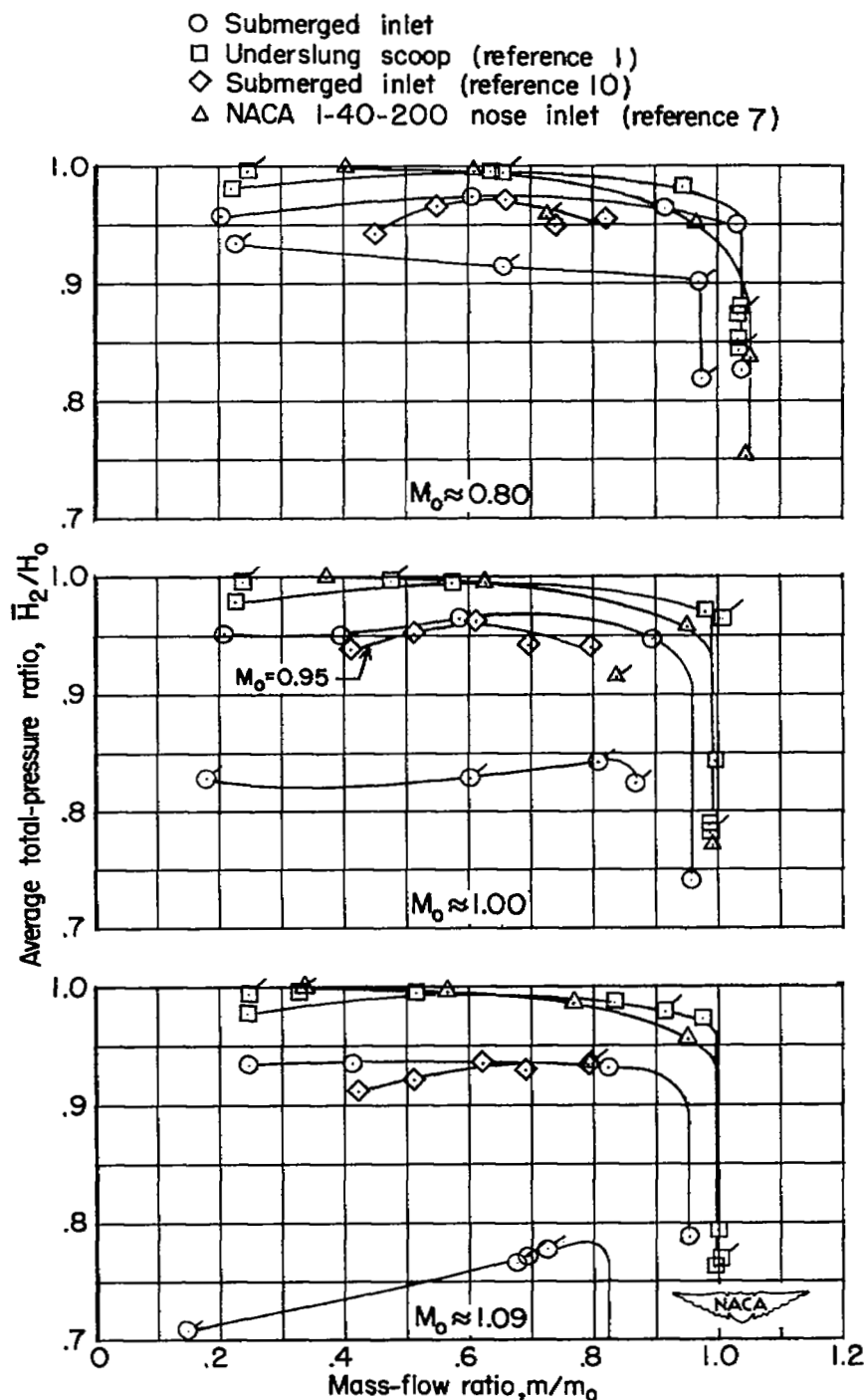several angles of attack.

○ Submerged inlet
□ Underslung scoop (reference 1)
◇ Submerged inlet (reference 10)
△ NACA 1-40-200 nose inlet (reference 7)

$M_0 \approx 0.80$

$M_0 = 0.95$

$M_0 \approx 1.00$

$M_0 \approx 1.09$

Average total-pressure ratio, $\bar{H}_2/H_0$

Mass-flow ratio, m/m_0

Figure 20.- Comparison of total-pressure recovery for the submerged
   inlet with an underslung scoop and a nose inlet. $\alpha = 0°$. (Flagged
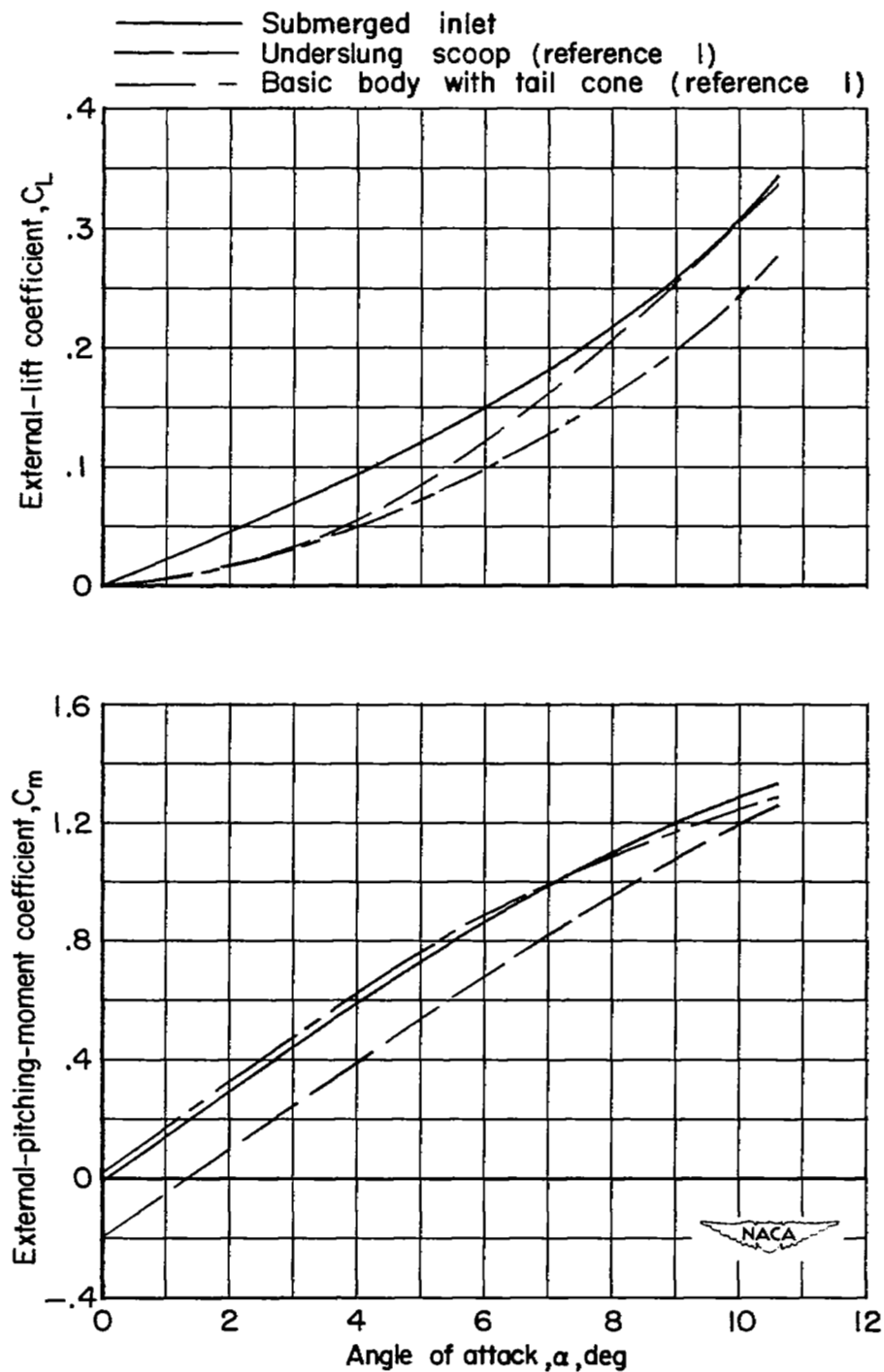   symbols for $\alpha \approx 10.6°$.)

Figure 21.- Comparisons of external lift and pitching moment of the submerged inlet with an underslung scoop and a basic body at $M_O = 0.95$ and $m/m_O = 0.80$.
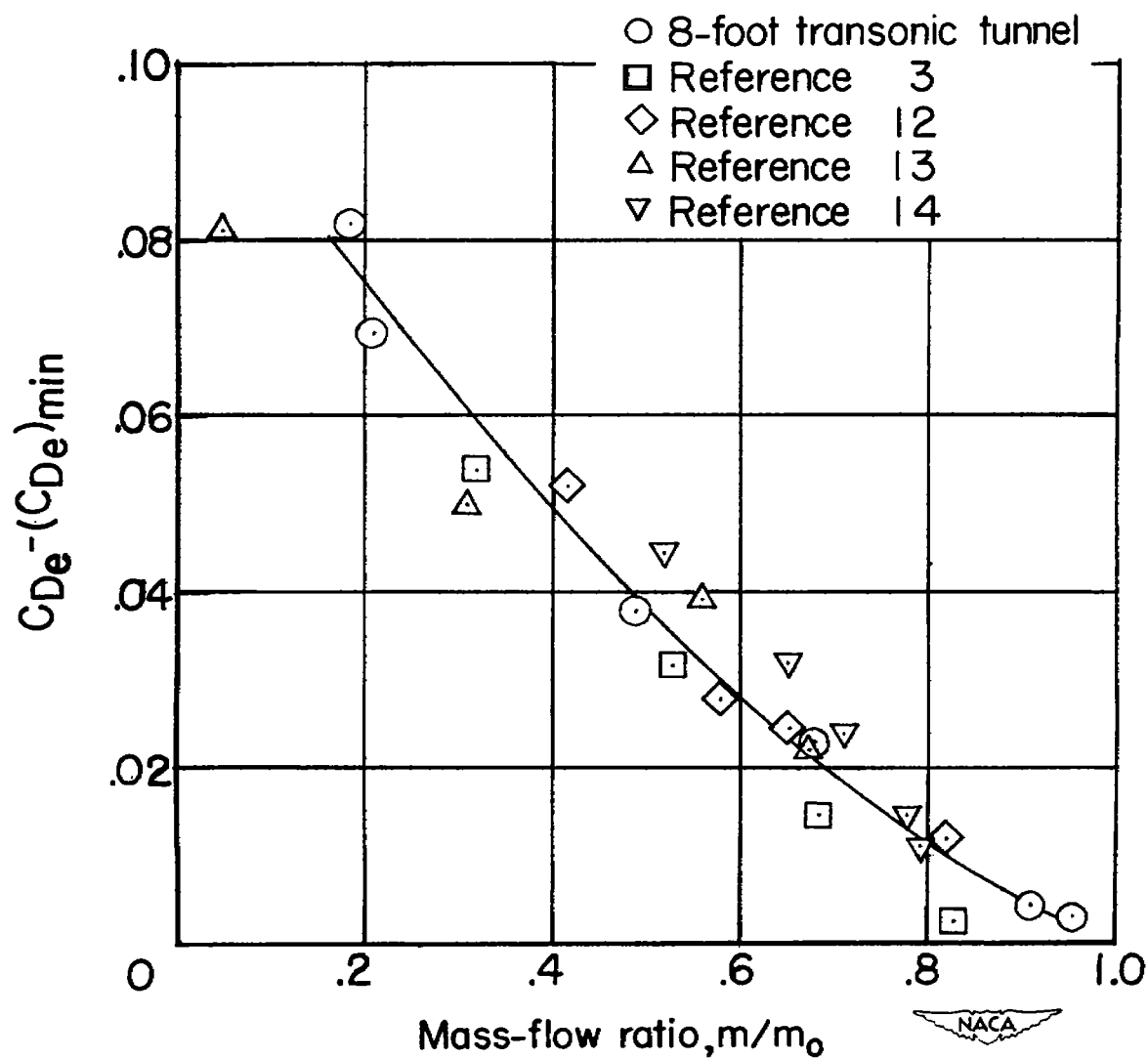
Figure 22.- Comparison of external-drag increment as a function of mass-flow ratio for several submerged inlets. $M_0 \approx 0.80$.
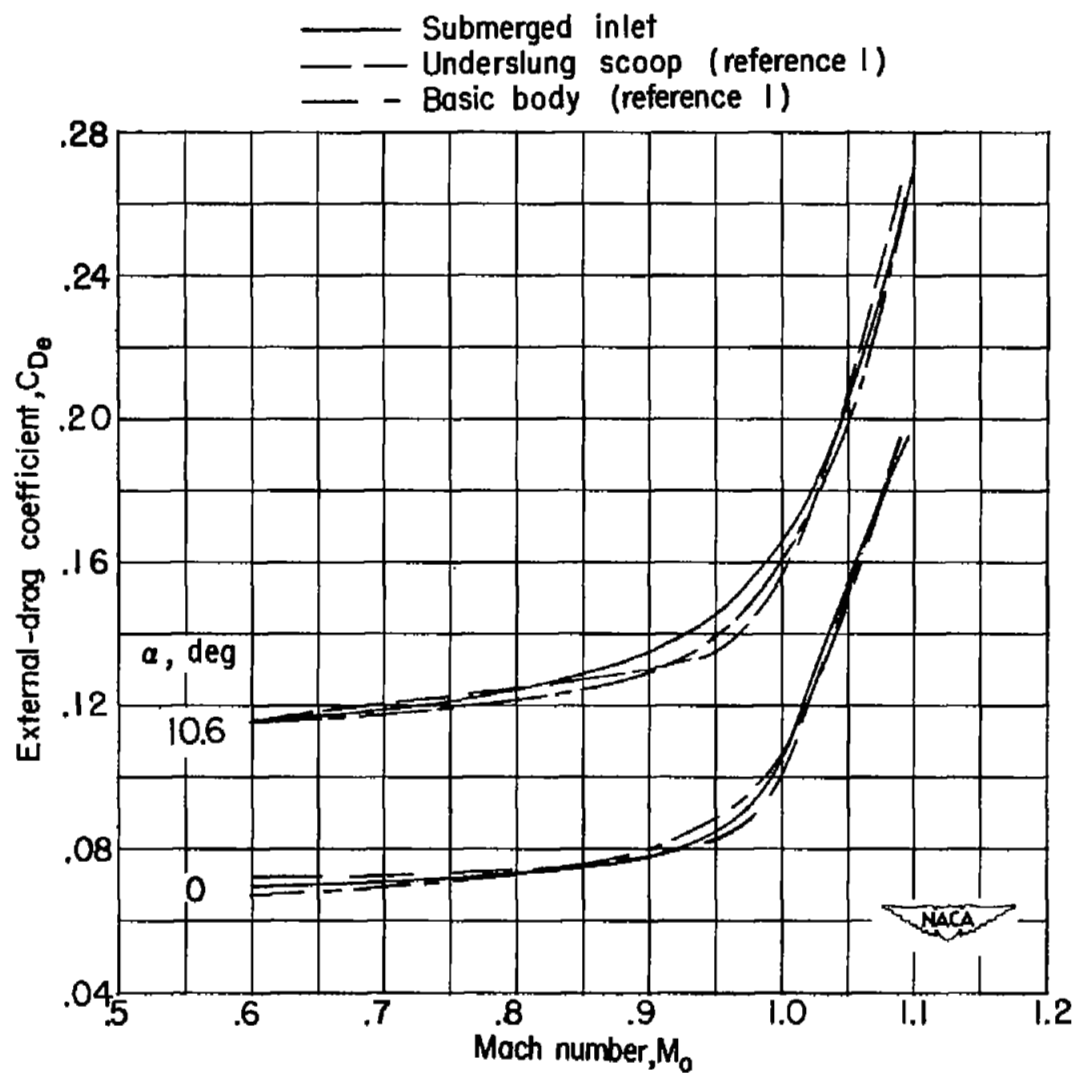
Figure 23.- Comparison of the plots of external-drag coefficient against Mach number for the submerged inlet. $m/m_O = 0.80$.